

COMPLEXITY ON SMALL SCALES III:  
IRON AND  $\alpha$  ELEMENT ABUNDANCES IN THE CARINA DWARF SPHEROIDAL GALAXY<sup>1</sup>

ANDREAS KOCH<sup>2,3</sup>, EVA K. GREBEL<sup>2,4</sup>, GERARD F. GILMORE<sup>5</sup>, ROSEMARY F.G. WYSE<sup>6</sup>,  
JAN T. KLEYN<sup>7</sup>, DANIEL R. HARBECK<sup>8</sup>, MARK I. WILKINSON<sup>9</sup>, AND N. WYN EVANS<sup>5</sup>  
akoch@astro.ucla.edu

*To appear in the Astronomical Journal*

ABSTRACT

We have obtained high-resolution spectroscopy of ten red giants in the Carina dwarf spheroidal (dSph) galaxy with the UVES spectrograph at the ESO Very Large Telescope in order to study the detailed chemical evolution of this Galactic satellite. Here we present the abundances of O, Na, Mg, Si, Ca, Ti and Fe. By comparison of the derived iron abundances  $[\text{Fe}/\text{H}]$  with metallicities based on the well established calcium triplet (CaT) calibration,  $[\text{Fe}/\text{H}]_{\text{CaT}}$ , we show that the empirical CaT technique yields good agreement with the high-resolution data for  $[\text{Fe}/\text{H}] \gtrsim -2$  dex, but tends to deviate from these data at lower metallicities. With  $[\text{Fe}/\text{H}] \sim -1.7$  dex the mean iron abundance of our targets is fully consistent with the peak metallicity of Carina as derived from medium-resolution spectroscopy and previous photometric studies, all calibrated onto iron via Galactic globular cluster scales. We identify two metal poor stars with iron abundances of  $-2.72$  and  $-2.50$  dex. These stars are found to have enhanced  $[\alpha/\text{Fe}]$  ratios similar to the elemental ratios of stars in the Milky Way halo. In this context it is conceivable that the moderately metal poor halo stars may originate from an early dSph accretion event. The bulk of the Carina red giants exhibit a depletion in the  $[\alpha/\text{Fe}]$  abundance ratios with respect to the Galactic halo at a given metallicity. One of our targets with a moderately low  $[\text{Fe}/\text{H}]$  of  $-1.5$  dex is considerably depleted in almost all of the  $\alpha$ -elements by  $\sim 0.5$  dex compared to the solar values. Such low values of the ratio of  $\alpha$ -elements to iron can be produced by stochastic fluctuations in terms of an incomplete mixing of single Type Ia and Type II supernova (SN) events into the interstellar medium. Moreover, the system's slow star formation (SF) rate grants sufficient time for SNeI to occur. Our derived chemical element ratios are consistent with the episodic and extended SF in Carina previously derived from analyses of its color-magnitude diagram. We find a considerable star-to-star scatter in the abundance ratios. This suggests that Carina's SF history varies with position within the galaxy, with incomplete mixing. In addition, or alternatively, the SF rate is so low that the high-mass stellar IMF is sparsely populated, as expected on statistical grounds in low-mass star clusters, leading to true scatter in the resultant mass-integrated yields. Both ideas are consistent with slow stochastic SF in dissolving associations or star clusters, so that one may not speak *prima facie* of a single "SF history" at a detailed level.

*Subject headings:* Galaxies: abundances — Galaxies: dwarf — Galaxies: evolution — Galaxies: stellar content — Galaxies: structure — Galaxies: individual (Carina) — Local Group

1. INTRODUCTION

Dwarf spheroidal galaxies (dSphs) are intriguing objects: they are the least luminous, least massive galaxies known (e.g., Grebel et al. 2003). They also appear to be the most dark-matter dominated objects (e.g., Gilmore et al. 2007 and references therein). For many years dSphs were considered the potential building blocks of larger galaxies, and thus potential key stones from which to extract the merging history of the Milky Way (e.g., Gallagher & Wyse 1994 and references therein). While there is clear evidence for past mergers of dwarf galaxies with the Milky Way, the age distributions and metallicity distributions of

stars in the dSphs, plus recent detailed abundance analyses (Grebel & Gallagher 2004; Venn et al 2004), have called a simple building block scenario in question. These limit accretion and merging of systems like the surviving dSphs to early epochs only (Unavane et al. 1996).

Among the dSphs orbiting the Milky Way the Carina dSph stands out because of its unusual star formation (SF) history. It is the only dSph to exhibit clearly episodic SF interrupted by long quiescent periods. Carina has been the subject of numerous, primarily photometric, studies (for an overview of past work, see Koch et al. 2006a; hereafter Paper I). We recently analysed Carina's metallicity distribution function (MDF) derived from medium-resolution

<sup>1</sup> Based on observations collected at the European Southern Observatory at Paranal, Chile; Large Programme proposal 171.B-0520(A).

<sup>2</sup> Department of Physics and Astronomy, Astronomical Institute of the University of Basel, Binningen, Switzerland

<sup>3</sup> UCLA, Department of Physics and Astronomy, Los Angeles, CA, USA

<sup>4</sup> Astronomisches Rechen-Institut, Zentrum für Astronomie Heidelberg, University of Heidelberg, Heidelberg, Germany

<sup>5</sup> Institute of Astronomy, Cambridge University, Cambridge, UK

<sup>6</sup> The John Hopkins University, Baltimore, MD, USA

<sup>7</sup> Institute for Astronomy, University of Hawaii, Honolulu, HI, USA

<sup>8</sup> Department of Astronomy, University of Wisconsin, Madison, WI, USA

<sup>9</sup> Department of Physics and Astronomy, University of Leicester, Leicester, UK

spectroscopy around the near-infrared Calcium II triplet (CaT) of 437 red giants (Paper I), from which we found a mean metallicity of  $[\text{Fe}/\text{H}]_{\text{CaT}} = -1.7$  dex on the scale of Carretta & Gratton (1997), with a wide range from about  $-3.0$  to  $0.0$  dex. Hence, there is evidence of considerable enrichment during the evolutionary life time of this dSph from about 12 Gyr ago to a few Gyr ago.

Low- to medium resolution spectroscopic studies are well suited to investigate the true, spectroscopic mean metallicity and metallicity spread of individual dSphs and to derive their MDF. Combined with photometry, this permits one to assess to what extent age and metallicity conspire (i.e., the age-metallicity degeneracy in color-space), to search for possible spatial gradients, and to explore the galactic evolutionary histories taking into account their chemical evolution. One should note that the overall ‘metallicity’, which is commonly represented via  $[\text{Fe}/\text{H}]$  or  $[\text{Fe}/\text{H}]_{\text{CaT}}$ , is generally most sensitive to the *integrated* past SF history (see, e.g., Paper I), while it is rather insensitive to the details of that SF history. Unravelling SF histories requires knowledge of individual elemental abundances and of the associated stellar ages: the evolution of specific chemical element ratios is intimately linked to the SF history of a galaxy, the initial mass function (IMF), and the binary fraction governing the rate of Supernovae (SNe) of Type Ia.

An important example of such abundance ratios is  $[\alpha/\text{Fe}]$ , which can be efficiently used as a “chemical clock” (Tinsley 1976; Wyse & Gilmore 1988; Matteucci 2003). The  $\alpha$ -elements (O, Mg, Si, Ca, Ti) form in quickly evolving high-mass stars, which end their lives in core-collapse SNe II. Fe is also synthesized in SNe II, but predominantly in SNIa, which occur on much longer time scales. Hence, modulo loss of metals from the galaxy, the  $[\alpha/\text{Fe}]$ -ratio of a stellar population records its SF history, reflecting the relative delay in the injection of Fe and  $\alpha$ -elements into the interstellar medium (Matteucci & Greggio 1986; Gilmore & Wyse 1998; Lanfranchi & Matteucci 2004; Lanfranchi et al. 2006; Robertson et al. 2005; Font et al. 2006).

Stars in dSphs have lower  $[\alpha/\text{Fe}]$  abundance ratios on average than do Galactic halo stars of the same metallicity (Shetrone, Côté & Sargent 2001; Fulbright 2002, Shetrone et al. 2003 [hereafter S03]; Tolstoy et al. 2003 [hereafter T03]; Geisler et al. 2005). This is generally interpreted as evidence of a low SF rate in dSphs compared to the Galactic halo, as predicted by Unavane et al. (1996). The actual values will sensitively depend on the SF and ISM mixing histories, and the IMFs, of both the dSph galaxy and of the formation location of the field halo stars.

From their analysis of five red giants in Carina, S03 and T03 deduce the imprints of SF bursts and pauses in Carina’s abundance patterns. Each SF burst can be expected to be accompanied by a rapid increase in  $[\alpha/\text{Fe}]$  (Gilmore & Wyse 1991, 1998), followed by a smoother decline in this ratio during any subsequent period of low SF. This simply reflects the continuing production of Fe in SNe Ia, which continue for many Gyr after the formation of their progenitor stars (Matteucci & Greggio 1986), with little  $\alpha$ -enrichment due to the paucity of SNe II. This SF and consequent enrichment history was claimed to be also reflected in variations of the heavy-element patterns, such as some  $[s/r]$ -process element abundance ratios vs.

metallicity. The illustrative scenarios proposed by S03 and T03 suggest an ancient epoch of SF (around 13 Gyr ago), a subsequent quiescent phase of some 3 Gyr, and another SF period approximately 7–11 Gyr ago. This is, however, not fully compatible with Carina’s detailed SF history as derived from color-magnitude diagram (CMD) modeling (e.g., Smecker-Hane et al. 1994; Mighell et al. 1997; Hurley-Keller et al. 1998; Monelli et al. 2003; Rizzi et al. 2003) and thus merits further investigation.

Our current study is a further step into this direction. We have enlarged the previously available sample by adding ten new stars, for which we obtained high-resolution spectra using the UVES spectrograph at the Very Large Telescope (VLT) of the European Southern Observatory. Considering the considerable expense in exposure time for high-resolution studies, this represents already a substantial improvement, even though these data still only yield snapshots in sampling the SF episodes of Carina. Each of our target stars provides a valuable picture of its local environment at the time of its formation. We have underway a much larger VLT/UVES study of Carina, to extend this work.

Calibration of the reduced width of the near-infrared CaT index in terms of metallicity is another issue involving an understanding of the abundance of the  $\alpha$ -elements. The widely used, empirical calibrations (Armandroff & Da Costa 1991; Rutledge et al. 1997a,b) are all based on the metallicity scales of Galactic globular clusters (e.g., Zinn & West 1984; Carretta & Gratton 1997; Kraft & Ivans 2003), themselves calibrated by iron elemental abundances derived from high-resolution echelle spectra. Cole et al. (2004) have extended this calibration to ages as young as 2.5 Gyr and metallicities in the range of  $-2.0 < [\text{Fe}/\text{H}] < -0.2$  dex so that even the metallicities of stars in dSphs with extended SF histories and prominent intermediate-age populations can be measured from the CaT. However,  $[\alpha/\text{Fe}]$  varies systematically across this range in the calibrators, so that it remains an open question whether and to what extent the extrapolation of the calibrations towards the metal-poor and metal-rich tails of the MDFs introduces a possible bias or significant deviations from the “true” Fe-line stellar metallicity. The CaT calibration explicitly assumes a  $[\text{Ca}/\text{Fe}]$  ratio that is similar to the one found in the Galactic globular clusters, i.e., a ratio of the order  $\sim +0.3$  dex (Carney 1996; McWilliam 1997; Pritzl et al. 2005). However, in dSphs this ratio is not an *a priori* known quantity, and generally this value shows a wide range, even within one galaxy. There is evidence that some stars in some dSphs can reach  $[\text{Ca}/\text{Fe}]$  values as enhanced as the Galactic halo (Shetrone et al. 2001, S03). Bosler et al. (2007) argue that the CaT line strength is naturally best mapped onto  $[\text{Ca}/\text{H}]$ , where the respective calibration is independent of the SF history of the system and valid over a broad range of metallicities and ages. Our measurements of  $[\alpha/\text{Fe}]$  in Carina will then aid in elucidating the validity and accuracy of traditional CaT metallicity measurements in the dSphs.

In this current study we focus on the abundance patterns for Na, Fe and the  $\alpha$ -elements O, Mg, Si, Ca, Ti in ten red giants in Carina. An analysis of the heavy element abundance ratios will be presented in a forthcoming paper (Koch et al., in preparation). In §2, we describe our data

and their reduction. §3 describes the atomic data and atmospheric parameters used in the abundance analysis including a detailed discussion of errors. In §4 we present our abundance results for iron and the individual  $\alpha$ -elements before discussing their implications for Carina’s chemical evolution in §5. §6 summarizes our findings.

## 2. DATA AND REDUCTION

Our data were obtained in the course of the ESO Large Programme 171.B-0520(A) (PI: G. F. Gilmore; see also Paper I; Wyse et al. 2006; Wilkinson et al. 2006; Koch et al. 2007, for details) that aims at studying the kinematic and chemical characteristics of Galactic dSphs. Two of these galaxies were extensively studied in medium resolution mode, namely Leo II (Koch et al. 2007) and Carina (Paper I). In parallel, a number of high-resolution spectra of red giants in Carina were obtained, in order to study the detailed chemical composition of this particular galaxy. To allow us to perform accurate chemical abundance studies at a high signal-to-noise (S/N) ratio within a reasonable integration time, 30 bright giants below the tip of the RGB were selected from the CMD, reaching V-band magnitudes slightly above 18 mag (see Table 1). Eleven of these stars were also observed with medium-resolution around the CaT region, from which we derived Carina’s MDF in Paper I. For these stars we can compare directly the stellar metallicities from the CaT calibration with the iron abundance from the high-resolution measurements, and thus assess the validity of the CaT calibration method.

### 2.1. Data acquisition

In parallel with the observing runs in December 2003 (see Paper I), during which medium-resolution spectroscopy of red giants in Carina was obtained, we used the high-resolution spectrograph UVES (Ultraviolet and Visual Echelle Spectrograph) at the ESO/VLT in multi-object mode. Using UVES in combination with the FLAMES fibre facility permits one to feed nine fibres to the UVES instrument, where we dedicated one fibre per setup to observing blank sky. This configuration facilitates the sky subtraction later on.

The FLAMES/UVES fibre mode has been designed for the red arm of the spectrograph. Our observations used the standard setup with a central wavelength of 580 nm, which gives a total spectral range of 470–680 nm. With a fibre aperture on the sky of 1'' and our chosen CCD binning of  $1 \times 1$  pixels the instrument provides a resolving power of  $\sim 47000$ .

### 2.2. Data reduction

The data were reduced using the standard UVES pipeline (Modigliani 2004<sup>10</sup>), which operates within the MIDAS environment<sup>11</sup>. The respective standard steps comprise bias subtraction and division by a master slit flat field. The definition of the spectral orders is obtained by the usual means of processing odd- and even-numbered

fibre flat field frames, combined with a first guess order position table from the Th-Ar wavelength calibration lamp. In the next step, the wavelength solution is determined via calibration exposures from this Th-Ar lamp, followed by the extraction of the target (and sky) spectra using an optimal extraction algorithm. The final extracted, wavelength-calibrated spectra with contiguously merged orders are then sky-subtracted using the dedicated sky spectrum taken in each setup. Finally, the individual exposures are shifted to the heliocentric standard of rest and coadded, weighted by the spectrum’s individual S/N. Typical S/N ratios of the final spectra achieved in this way are approximately  $20 \text{ pixel}^{-1}$ .

### 2.3. Membership estimates

The likely Carina membership of the target stars was assessed by means of their radial velocities. We generated a template spectrum from a line list comprising 101 strong absorption features with equivalent widths (EWs) as expected for typical red giant spectra in dSphs. Cross-correlation of the observations against this template using IRAF’s<sup>12</sup> *fxcor* task finally yielded accurate radial velocities with a median uncertainty of  $0.9 \text{ km s}^{-1}$ .

For the 11 targets for which we also obtained medium-resolution spectra of the CaT region, the velocity measurements from the UVES spectra are in excellent agreement with the velocities derived from the CaT (see Paper I) to within their uncertainties, and we find a median offset between both estimates of  $0.5 \text{ km s}^{-1}$  with a  $1\sigma$ -scatter of  $1.1 \text{ km s}^{-1}$ .

Out of our 30 targets, 12 stars clearly peak at Carina’s systemic velocity around a mean of  $225 \text{ km s}^{-1}$  with a dispersion of  $6.4 \text{ km s}^{-1}$ . This is in good agreement with Carina’s radial velocity distribution (Mateo 1998; Majewski et al. 2005; Paper I). The remaining 18 targets have radial velocities that deviate by more than  $120 \text{ km s}^{-1}$  from this mean, which corresponds to  $20\sigma$  and unambiguously rules out their membership in Carina. These stars are not considered in the current study and are likely Galactic interlopers (Wyse et al. 2006). We note that the candidates for observation were selected deliberately to extend well to the blue and to the red of the Carina RGB, so that any very metal-poor or metal-rich Carina stars would be included. No such stars were found. Two of the radial velocity members were identified as carbon stars via their strong molecular bands. These spectra were omitted from the abundance analyses presented here.

## 3. ABUNDANCE ANALYSIS

For the abundance determinations, we employed the common technique of an EW analysis. For this purpose, we used the 2002 version of the stellar abundance code MOOG (Sneden 1973), in particular using its *abfind* driver. For the van der Waals line damping, the standard Unsöld approximation was adopted within MOOG.

The accurate derivation of stellar abundance ratios sensitively relies on the choice of proper atomic data, in par-

<sup>10</sup> This document is available online via

<http://www.eso.org/projects/dfs/dfs-shared/web/vlt/vlt-instrument-pipelines.html>.

<sup>11</sup> The European Southern Observatory Munich Image Data Analysis System (ESO-MIDAS) is developed and maintained by the European Southern Observatory.

<sup>12</sup> IRAF is distributed by the National Optical Astronomy Observatories, which are operated by the Association of Universities for Research in Astronomy, Inc., under cooperative agreement with the National Science Foundation.

ticular the oscillator strengths. Concern about using solar  $gf$ -values for the analysis of our late-type red giant target stars prompted us to perform a differential abundance analysis relative to Arcturus ( $\alpha$  Boo), a bright K1.5 disk giant of only moderate metal-deficiency ( $[\text{Fe}/\text{H}] = -0.50$  dex) and with atmospheric parameters very similar to those expected for the Carina red giants of our sample (e.g., Peterson et al. 1993; Friel et al. 2003; Fulbright et al. 2006, 2007; Koch & McWilliam 2008). For this purpose, we used the Arcturus spectral atlas of Hinkle et al. (2000) to obtain a set of reference measurements.

### 3.1. Equivalent widths and $gf$ -values

In order to identify suitable transitions for our abundance determinations, we compiled a line list from various literature sources. Essentially, we exploited the compilations from the bulge giant and thick disk star studies of McWilliam et al. (1995) and Prochaska et al. (2000), from which we assembled a number of absorption features for a number of chemical elements (see references in these works for the sources of the respective atomic data). We chose the lines with the least amount of stellar and telluric contamination, which thus appear reasonably unblended.

The EWs of these lines were measured using IRAF's *splot*-task assuming a single Gaussian line profile. Typical *splot*-errors on the widths are of the order of 5% (a few mÅ), and the EWs of those lines in common with Fulbright et al. (2006, 2007) agree to within 3% with their measurements.

The oscillator strengths used in the majority of abundance studies are nowadays based on laboratory measurements, such as the O'Brian values (O'Brian et al. 1991), Hannover measurements (Bard & Kock 1994) or the Oxford  $gf$ -values (Blackwell et al. 1995), all of which are employed in the work of McWilliam et al. (1995) and Prochaska et al. (2000). Still, as Prochaska et al. (2000) note, even with such maximally accurate laboratory measurements at hand, the  $gf$ -values impose a major error source in red giant abundance studies, particularly when referencing one's abundances to the solar meteoritic (Anders & Grevesse 1989) or the updated empirical (Grevesse & Sauval 1999; Asplund et al. 2005) solar abundance reference frame. Therefore we have chosen to conduct our analysis differentially with respect to the well-studied red giant Arcturus, thus minimizing the uncertainties associated with solar and laboratory  $gf$ -values. Since Arcturus exhibits atmospheric properties similar to the stars of our own study, such an analysis will also aid the reduction of systematic errors, such as a priori unknown deficiencies in the model atmospheres or the influence of weak, unknown blends, which might scale with metallicity (e.g., Fulbright et al. 2006). To this end we measured the EWs of the lines in Arcturus from the high-quality spectral atlas of Hinkle et al. (2000).

Adopting the well established atmospheric parameters of  $\alpha$  Boo ( $T_{\text{eff}} = 4290$  K,  $\log g = 1.55$ ,  $\xi = 1.67$  km s $^{-1}$ ,  $[\text{Fe}/\text{H}] = -0.5$ ) from Fulbright et al. (2006) and our measured EWs, we derived the  $gf$ -values on a line-by-line basis in order to reproduce each element's abundance from

Fulbright et al. (2006, 2007). As a result, our Arcturus-based oscillator strengths agree with the laboratory values to within  $\sim 8\%$  on average. The full line list is given in Table 2, together with the respective EW measurements for each star.

### 3.2. Model Atmospheres and stellar parameters

Throughout our analyses we interpolated the model atmospheres from the updated grid of R. L. Kurucz's<sup>13</sup> one-dimensional 72-layer plane-parallel line-blanketed models with the convective overshoot option switched off and assuming that local thermodynamic equilibrium (LTE) holds for all species. Moreover, our model calculations incorporated the new opacity distribution functions, ODFNEW, provided by F. Castelli<sup>14</sup> (Castelli & Kurucz 2003) for the Carina stars, assuming scaled-solar elemental abundances, and the respective  $\alpha$ -element enhanced models, AODFNEW, for Arcturus. The latter are necessary since it is known that Arcturus exhibits a considerable enhancement in these elements (Peterson et al. 1993; Fulbright et al. 2007) of  $[\alpha/\text{Fe}] \sim +0.4$  dex.

The initial estimates for the stellar effective temperatures were derived using dereddened colors from the photometry obtained by the ESO Imaging Survey (EIS<sup>15</sup>; Nonino et al. 1999; Paper I), complemented by infrared colors, which were drawn from the Point Source Catalogue of 2MASS (Cutri 2003). For Carina, we use a reddening of  $E(B-V) = 0.06$  (Mighell 1997), which is also consistent with the value we found from the extinction maps of Schlegel et al. (1998). To correct the infrared colors, the respective reddening relations from Cardelli et al. (1989) were applied. Finally, photometric effective temperatures were calibrated using the empirical relations derived by Alonso et al. (1999, 2001). Since the Alonso et al. calibrations of  $B-V$  and  $V-K$  require colors in the Johnson-Cousins (JC) system, we employed the photometric transformations described in Paper I in order to convert the input  $B$  and  $V$  magnitudes from the photometric system of the EIS to the standard JC system. The 2MASS  $K$ -band magnitude was transformed to the Bessel & Brett (1988) homogenized system, using the equations provided by the Explanatory Supplement to the 2MASS All Sky Data Release (Cutri 2003). Since this transformation includes two steps of calibrations, i.e., from the 2MASS to the CIT system and from CIT to the Bessel & Brett (1998) system, the transformation errors from both calibrations have to be incorporated to yield the final photometric uncertainty of the colors (see also Sivarani et al. 2004). Table 3 lists the photometric properties of all target stars with radial velocities that are consistent with membership in Carina.

As initial guesses for the metallicity to be used in the  $T_{\text{eff}}$  calibrations and in the model atmospheres we adopted the value derived from our CaT study of Paper I for the six member stars in common. Otherwise Carina's mean metallicity of  $-1.7$  dex (Paper I) was assumed for the remaining four red giants for which no metallicity measurement was available.

In practice, we adopted the  $T_{\text{eff}}(V-K)$  value as the final stellar photometric temperature, since the large wave-

<sup>13</sup> These atmosphere grids can be downloaded from <http://cfaku5.cfa.harvard.edu/grids.html>

<sup>14</sup> See <http://wwwuser.oat.ts.astro.it/castelli>.

<sup>15</sup> The reduced and calibrated photometry is available from the EIS Web pages, see <http://www.eso.org/science/eis/>.

length baseline of this color index makes this temperature the least susceptible to the underlying photometric uncertainties, yielding the most accurate results. The temperatures obtained from the B–V colors are systematically cooler than their respective V–K counterparts by  $\sim 70$  K on average. The random errors on the effective temperature, based on the full photometric uncertainties, amount to 70 K on average.

The stellar surface gravities,  $\log g$ , were initially determined using the basic stellar structure equations

$$\log \frac{g}{g_{\odot}} = \log \frac{M}{M_{\odot}} + 4 \log \frac{T_{\text{eff}}}{T_{\text{eff},\odot}} - 0.4 (M_{\text{bol},\odot} - M_V - \text{BC}), \quad (1)$$

where we adopted  $T_{\text{eff},\odot} = 5777$  K,  $M_{\text{bol},\odot} = 4.74$  and  $\log g_{\odot} = 4.44$  and a distance of Carina of 94 kpc (Mighell 1997). Moreover, the photometric temperature as derived above was used in this relation, and the stellar mass was taken to be  $0.8 M_{\odot}$ , in correspondence to the typical main-sequence turn-off mass. The bolometric correction (BC) was obtained by interpolation of the respective Kurucz-atmosphere grids.

Adopting this set of values as the input parameters, the final spectroscopic parameters were determined from a subset of the clean Fe I lines listed in Table 2, for which  $-5.4 \lesssim \log_{10}(\text{EW}/\lambda) \lesssim -4.5$ , corresponding to a range of  $\sim 20$  to  $160 \text{ m}\text{\AA}$  at  $5000 \text{\AA}$ . The lower limit of this selection prevents weak lines being spuriously detected, thus artificially raising the mean iron abundance near the cut-off. The strongest, saturated lines were pruned from the list, since they do not lie on the linear part of the curve of growth and are predominantly formed in the highest layers, where the atmosphere models become progressively unreliable (McWilliam et al. 1995; Johnson 2002).

Atmospheric parameters were determined by iteratively modifying the models to satisfy three constraints in successive steps. As a first step, we determined the microturbulent velocity  $\xi$ . For this purpose abundances from the neutral iron lines were iteratively calculated, demanding that there is no trend of abundance with the reduced width  $\text{EW}/\lambda$ . The scatter around the zero slope from a least-squares fit was then taken as a measure of the uncertainty on the microturbulent parameter. In this way, we conservatively obtain typical accuracies of  $0.1 \text{ km s}^{-1}$  on  $\xi$ .

In the second step, spectroscopic temperatures were obtained by requiring excitation equilibrium. Based on the range of  $T_{\text{eff}}$  that produces acceptable fits in the Fe I-abundance versus excitation potential (EP) plot, we estimate the typical errors of the spectroscopic temperature to be  $\pm 100$  K, slightly larger than the photometry-based errors. Generally, our spectroscopic  $T_{\text{eff}}$ -values are systematically higher than the photometric estimates, and we note an offset of  $+250$  K on average for our standard atmospheres. For some of the targets this discrepancy can be as high as 500 K. Although a systematic offset of  $\sim 250$  K may raise some concern, differences between the spectroscopic temperature scales do not come as a surprise (see also the discussion in Johnson 2002). In our analyses we use the spectroscopic temperatures to define the atmospheric  $T_{\text{eff}}$  for several reasons. First, the photometric errors of the infrared colors are rather high. The median photometric uncertainty of our targets from 2MASS amounts to 0.1 mag in V–K. A reddening uncertainty of

0.1 mag leads to a  $T_{\text{eff}}$  variation of  $\pm 100$  K. It turns out that an unreasonably large systematic decrease of 0.4 mag on average in V–K (up to 0.71 mag for the most deviant stars), be it due to photometric or reddening uncertainties, would be required to reconcile the spectroscopic and photometric temperatures. However, this would correspond to an unreasonably large increase of Carina’s distance modulus of 0.45–0.8 mag (reflecting a distance shift of  $\sim 18$ –30 kpc). Inconsistent photometric and spectroscopic  $T_{\text{eff}}$ -values could occur due to errors in the  $gf$ -values, which may correlate with the EP (Johnson 2002). However, this has been shown not to be the case either for laboratory oscillator strengths (e.g., Blackwell et al. 1995), nor should it be a problem in our differential line-by-line analysis. Finally, Johnson et al. (2006) have shown that the use of a photometric  $T_{\text{eff}}$  yielded highly diverging non-standard abundance ratios for their sample of old red giants in LMC clusters, again strengthening our confidence in the use of the spectroscopic values.

In the third step, the appropriate surface gravity for each star was constrained by assuming ionization equilibrium, thus requiring that the  $\log g$ -sensitive Fe II abundance matches the abundance from the Fe I lines,  $\varepsilon(\text{Fe I})$ . These abundances were repeatedly computed for both species with  $\log g$  varying in small steps until the results from both ionization stages agreed reasonably well. By demanding that both ionisation levels do not deviate by more than 0.1 dex we could effectively constrain our gravity estimate to within an accuracy of  $\pm 0.2$  dex.

As for the case of  $T_{\text{eff}}$ , the gravities determined from ionization equilibrium are also systematically higher than the photometrically derived values (eq. 1). This discrepancy cannot be resolved by adopting our spectroscopic  $T_{\text{eff}}$ -values in eq. 1 instead of the color temperatures. This would render the gravities larger by  $\sim 0.18$  dex on average, which is still lower than their spectroscopically derived values. It is feasible that this is due to a mild degeneracy of the entire parameter set, where a fraction of the offset can be explained by discrepancies in the adopted temperature. Since an increase in  $T_{\text{eff}}$  decreases the difference between  $\varepsilon(\text{Fe I})$  and  $\varepsilon(\text{Fe II})$ , one inevitably derives an increased stellar gravity. Due to this interdependence, a change in  $\log g$  entails a slight change in the slope of the EP plot, which again is reflected by another rise in effective temperature (e.g., McWilliam et al. 1995; Johnson 2002; Johnson et al. 2006; Fulbright et al. 2006; see also Section 3.3). Microturbulence also has an influence on  $\log g$ , though to a lesser extent. While matching  $\varepsilon(\text{Fe I})$  and  $\varepsilon(\text{Fe II})$  to achieve ionization equilibrium itself can be done accurately, one should also keep in mind that there is only a small number of stronger and well determined Fe II transitions available in our spectra and in the literature. On average, we have only about four Fe II lines at hand, which will not only lead to larger random errors on the derived  $[\text{Fe II}/\text{H}]$  values, but also frustrate accurate gravity estimates. As we will show in the next Section, even a implausibly large variation of  $\log g$  has an only marginal effect on the abundances, in particular since we primarily rely on the neutral iron lines to assign the stellar  $[\text{Fe}/\text{H}]$ .

The entire parameter determination for  $\xi$ ,  $T_{\text{eff}}$  and  $\log g$  was successively iterated to approach simultaneous convergence, adopting the Fe I abundance from the last iteration

as the input metallicity  $[M/H]$  (which strictly accounts for the global metal abundance, e.g., Salaris et al. 1993) for the subsequent atmosphere calculation. The final atmospheric parameters for each star derived in this way are tabulated in Table 3. With this final optimized parameter set, the abundance of the ionized state Fe II deviates by no more than 0.04 dex from the Fe I abundance, with an average deviation of  $\sim 0.01\text{--}0.02$  dex.

### 3.3. Abundance errors

In order to determine accurate error estimates in the individual abundance ratios, we investigated the effects of the random uncertainties in the atmospheric parameters. First of all, abundance ratios were obtained for ten different model atmospheres for two stars (LG04c.000777 and LG04d.006628). These two stars were chosen because of their significantly different stellar parameters. In each of the models, the stellar parameters were separately varied by their typical random  $1\sigma$  uncertainty, as conservatively estimated in the previous Section. In Table 4 the differences of the abundance ratios for each of these models are given, i.e., for  $T_{\text{eff}} \pm 100$  K,  $\xi \pm 0.1$  km s $^{-1}$ ,  $\log g \pm 0.2$  dex and  $[M/H] \pm 0.2$  dex, w.r.t the values obtained from the atmospheres computed with the best spectroscopic parameter set.

At this stage of the analysis our model atmospheres for the Carina stars incorporate opacity distribution functions assuming scaled-solar element abundances (ODFNEW). It is important, however, to keep in mind that the  $\alpha$ -elements are important electron donors in the atmospheres of red giants. These metals supply a significant number of free electrons, which sustain the formation of  $H^-$  – the dominant source of the continuum opacity in these stars. It cannot be assumed *a priori* that the Carina stars exhibit any kind of enhancement in these elements, but measurements in seven dSphs of the Local Group, also comprising five stars in Carina (which do not coincide with our sample), indicate that many stars in these galaxies are in fact enhanced in a number of  $\alpha$ -elements (Shetrone et al. 2001, S03; Sadakane et al. 2004; Venn et al. 2004; Geisler et al. 2005). Therefore we additionally derived abundances under the assumption of an  $\alpha$ -enhancement of +0.4 dex in the atmospheres, by calculating models with the stellar default parameters, now using the  $\alpha$ -enhanced opacity distributions, AODFNEW (see, e.g., Fulbright et al. 2006, 2007). The change in each elements’ abundance ratio derived with this atmosphere from the standard atmosphere’s value is given in Table 4 in the column labeled “ $\alpha$ ”.

The model parameters are not independent but rather intricately correlated in several ways (McWilliam et al. 1995). This leads to covariances of the parameters’ uncertainties, which can be particularly significant for the case of  $T_{\text{eff}}$  and  $\log g$  caused by an explicit temperature-gravity dependence. A change in  $T_{\text{eff}}$  can also introduce a slope in the abundance vs. EW relation, which is used to fix  $\xi$ .

To quantify the covariances of the stellar parameters, we follow the prescription of Johnson (2002), which is, in turn, based on the formalism of McWilliam et al. (1995). For the representative stars LG04c.000777 and LG04d.006628 we start by drawing 20 random temperature values from a Gaussian with their spectroscopic  $T_{\text{eff}}$  as mean and with a dispersion of 100 K. For each of these,  $\log g$  was changed

accordingly, to reinstall ionization equilibrium. The resulting covariance

$$\sigma_{T \log g} = 1/N \sum_{i=1}^N (T_i - \langle T \rangle)(\log g_i - \langle \log g \rangle)$$

amounts to 40, with a correlation coefficient of 0.79, i.e., the mutual influences of temperature and gravity on our abundances are in fact highly correlated. Likewise, we computed 20 values for the microturbulence with a dispersion of  $0.1$  km s $^{-1}$  and readjusted the gravity of the atmosphere to regain ionization equilibrium. These parameters are less correlated, with  $\sigma_{\xi \log g} = -0.005$  and a correlation coefficient of 0.44. It turns out that covariance terms including the atmospheres’ metallicity  $[M/H]$  are negligible so that we did not include the respective mixed terms in the analysis.

Finally, we account for random errors in the EW measurements by computing the  $1\sigma$  scatter in the abundances, weighted by the square root of the number of absorption features,  $N$ , used in the derivation of  $\varepsilon$  (e.g., Carretta 2006). This statistical error,  $\sigma_{\text{EW}}/\sqrt{N}$ , (see also Table 5) accounts in principle for the line-to-line scatter and input atomic parameters. For those elements, for which only one absorption feature was measurable in the spectra, we adopted a representative error on the abundance through repeatedly varying the EW in the abundance determination within its typical accuracy (of the order of 5–10%). In general, for those elements with  $N \gtrsim 5$ , which is the case for our Ca-, Ti I- and Fe-lines, the total abundance error is dominated by the uncertainties in the atmospheric parameters (Prochaska et al. 2000). The major error source in terms of atmospheric parameters is in this case the temperature sensitivity. For elements with few lines, there is a progressively larger contribution of EW errors due to enhanced noise, unresolved blends or uncertainties in the continuum placement. Interestingly, neglecting  $\alpha$ -enhancement does not significantly alter any of the derived abundance ratios and only has a significant effect on the ionized species Ti II and Fe II, where the enhancement tends to overestimate the abundances by  $\sim 0.1$  dex.

The total uncertainty  $\sigma_{\text{tot}}$  of each elemental abundance ratio  $[X/H]$  due to random errors in the atmospheric parameters (listed in Table 5) is then obtained by summing the uncorrelated contributions from each individual parameter ( $T_{\text{eff}}$ ,  $\xi$ ,  $\log g$ ,  $[M/H]$ ,  $\alpha$ ,  $\Delta\text{EW}$ ) in quadrature, and adding the respective covariant contributions from  $T_{\text{eff}}$ ,  $\xi$  and  $\log g$  (see eq. 2 in Johnson 2002). Since variations in the atmospheres will affect different elements to a different extent, one has to additionally consider their covariances in computing the abundance ratios  $[X/Fe]$ . Therefore we obtain  $\sigma_{[X/Fe]}^2 = \sigma_X^2 + \sigma_{\text{Fe}}^2 - 2\sigma_{X\text{Fe}}$  with the covariance  $\sigma_{X\text{Fe}}$  according to eq. 6 from Johnson (2002). As a result, the typical error on our derived  $[\text{Fe I}/H]$  amounts to  $\sim 0.17$  dex and ranges from  $\sim 0.05$  to  $\sim 0.20$  dex for the other elements, while the uncertainty on  $[\text{O}/\text{Fe}]$  can be as high 0.35 dex.

Finally, we note that none of our abundances has been corrected for NLTE effects. Since our results will be compared below with similar LTE analyses (e.g., S03; Venn et al. 2004), this source of uncertainty will not be systematic on the whole. Despite our enforcement of ionization

equilibrium by reconciling  $\varepsilon(\text{Fe I})$  and  $\varepsilon(\text{Fe II})$ , the neutral and ionized species of Ti show a marginal difference of  $-0.12 \pm 0.18$  dex. If we demanded ionization equilibrium for the Ti lines to establish a  $\log g$ , our spectroscopic surface gravities would have had to be lower by 0.13 dex on average, which is well within our estimate of the uncertainty on this atmospheric parameter (see Section 3.2). The fact that our data do not exhibit any significant trend of  $\varepsilon(\text{Ti I})$  or  $\varepsilon(\text{Ti II})$  with  $T_{\text{eff}}$  nor with metallicity, supports our view that we can, for the moment, neglect NLTE effects in our analyses (Luck & Bond 1985; cf. Johnson 2002).

#### 4. RESULTS

Table 5 shows the final abundance ratios  $[X/\text{Fe}]$  ( $[\text{Fe}/\text{H}]$  for the iron lines themselves) for each chemical element  $X$ . These ratios are given w.r.t. the mean abundance of the neutral iron lines,  $\varepsilon(\text{Fe I})$ . Also tabulated are the number of lines,  $N$ , used to determine the unweighted mean abundance ratio for each element and standard deviation of each  $\varepsilon$  measured from these lines.

##### 4.1. Iron

The mean iron abundance of the red giants in Carina obtained from our high-resolution spectra is  $-1.69$  dex with a standard deviation of 0.51 dex. This is in excellent agreement with the mean of  $-1.72$  (on the scale of Carretta & Gratton 1997) derived from the CaT measurements. Also S03 find a mean of  $-1.64$  with a scatter of 0.2 dex from their high-resolution analysis of five red giants, while Smecker-Hane et al. (1999) reported a slightly lower value of  $-1.99$  dex from a small number of stars with CaT measurements. From this point of view, our targets can be considered as Carina members representing the typical metallicity range in this dSph.

There are some mildly metal-rich targets, which reach  $[\text{Fe}/\text{H}]$  of  $-1.27$  dex. Furthermore, we detect two metal-poor stars with  $[\text{Fe}/\text{H}] < -2.5$  dex, which contribute to the metal-poor tail of Carina’s MDF. These stars lie  $1.5$ – $2\sigma$  below the peak of the MDF. Nevertheless, this small number of metal-poor objects is not sufficient to resolve the apparent G-dwarf problem (or in fact “K-giant problem”, Koch et al. 2007) in dSphs (Smecker-Hane et al. 1999; Pont et al. 2004; Tolstoy et al. 2004; Venn et al. 2004; Helmi et al. 2006; Paper I; Bosler et al. 2007; Koch et al. 2007). Interestingly, at 1.4 and 2 core radii, these two stars are also located at the largest radial distances in our sample, thus matching the mild radial abundance gradient that was detected in Paper I (see also Harbeck et al. 2001). Recall that our parent sample selected for spectroscopy was three times larger than the eventual member sample, and was selected to ensure that any very metal-poor or metal-rich member star would be included. The absence of such stars from our sample then indicates a real scarcity.

##### 4.1.1. Assessing the CaT calibration

The six stars that were observed in both low- and high-resolution mode enable us to assess the accuracy of the calibration of the CaT abundance scale onto iron, since these stars cover a range of abundances. Fig. 1 shows a comparison of the estimates from both methods.

As the dashed line of unity in Fig. 1 (top panel) implies, all of the five more metal-rich red giants show good consistency between their CaT metallicity (on the scale of Carretta & Gratton 1997) and the high-resolution iron abundance, not deviating by more than  $0.8\sigma$  from unity. This range of metallicities is well sampled by the Galactic globular clusters (GGCs) in the calibrations of Rutledge et al. (1997a,b). An oft-cited caveat against calibrating the CaT in dSphs to a *Galactic* reference system is that GGCs tend to exhibit enhanced  $[\text{Ca}/\text{Fe}]$  ratios of  $\sim +0.4$  dex on average (e.g., Pritzl et al. 2005), while *dSph* stars show lower values in this ratio (Venn et al. 2004). As we will show in Sect. 4.3, our Carina dSph stars exhibit slightly lower  $[\text{Ca}/\text{Fe}]$  ratios of the order of  $+0.09 \pm 0.14$  dex, which should result in systematically lower line strengths of the CaT compared to the GGCs. A number of clusters in the Rutledge et al. (1997b) sample show in fact lower  $[\text{Ca}/\text{Fe}]$  values of  $\sim +0.1$  dex at metallicities similar to that of our Carina stars (e.g., Cohen & Meléndez 2005), and the GGCs, from which we derived the calibration of the CaT to  $[\text{Fe}/\text{H}]_{\text{CaT}}$  in Paper I, possess an average, enhanced,  $[\text{Ca}/\text{Fe}]$  of  $+0.21 \pm 0.11$  dex. Thus we might expect an inferred  $[\text{Fe}/\text{H}]_{\text{CaT}}$  lower by  $\sim 0.12$  dex with respect to the  $[\text{Fe}/\text{H}]$  abundance, based on the difference in  $[\text{Ca}/\text{Fe}]$  between target and calibrators (see also discussions in Paper I; Bosler et al. 2007). We find that our CaT based measurements are more metal poor by  $(0.08 \pm 0.09)$  dex on average. This small zero point shift is consistent with the above difference in  $[\text{Ca}/\text{Fe}]$  of the calibration clusters and target stars. Note that there is no obvious trend of the difference between high-resolution  $[\text{Fe}/\text{H}]$  and  $[\text{Fe}/\text{H}]_{\text{CaT}}$  with  $[\text{Ca}/\text{Fe}]$  discernible in our data.

The iron abundance of our metal-poor star is, at  $-2.50$  dex, lower by 0.44 dex ( $2.1\sigma$ ) than the CaT value. This deviation is in qualitative agreement with the CaT vs. high-resolution  $[\text{Fe}/\text{H}]$  comparison of a large number of dSph stars of Battaglia et al. (2008), who show that a systematic overestimate of the CaT abundances sets in below  $[\text{Fe}/\text{H}] \lesssim -2.2$  dex. Such a trend points to a general shortcoming of the method to reliably infer iron metallicities from the CaT index in the most metal poor red giants. Since the globular clusters in the sample of Rutledge et al. (1997b) “only” comprised a metallicity range from  $-0.64$  down to  $-2.02$  dex (Carretta & Gratton [1997] scale), measurements of stars beyond these limits necessarily rely on an extrapolation of the calibrations. In particular, the clusters employed for our calibrations in Paper I span a range from  $-2.0$  to  $-1.12$  dex.

As an additional test, we calibrated our GGC measurements from Paper I onto the Fe II scale of Kraft & Ivans (2003). The major difference to the old calibration lies in the  $[\text{Fe}/\text{H}]$  value for the cluster M68, for which Kraft & Ivans (2003) find a more metal poor  $[\text{Fe}/\text{H}]$  of  $-2.43$  dex, while this cluster has a metallicity of  $-2$  dex on the previously used scale of Carretta & Gratton (1997). In general, Carretta & Gratton (1997) have reported the most metal poor GGCs to be considerably more metal rich than other studies. The main impact of the new calibration (see bottom panel of Fig. 1) is that the most metal poor of our targets becomes even more deficient, at  $[\text{Fe}/\text{H}]_{\text{CaT}} \sim -3.1$  dex, which underestimates the metallicity compared to our high-resolution measurement by 0.56

dex. On average, the CaT measurements on the Kraft & Ivans (2003) scale are more metal poor by 0.3 dex than the UVES data, with a standard deviation of 0.12 dex around unity. Although Cole et al. (2004) and, more recently, Carrera et al. (2007), have demonstrated that the CaT technique is generally applicable for a broad age range of 0.25–13 Gyr and across a wide metallicity range spanning  $-2.2 < [\text{Fe}/\text{H}] < +0.47$ , the MDFs’ metal-poor tails remain unsatisfactorily sampled in most high resolution studies. The question of whether the metal-poor extensions of the MDFs of dwarf galaxies based on the CaT below  $\sim -2.2$  to  $-2.5$  dex, which are reported throughout the literature (e.g., Smecker-Hane et al. 1999; Tolstoy et al. 2001; Bosler et al. 2007; Pont et al. 2004; Tolstoy et al. 2004; Cole et al. 2004, 2005; Paper I) are then reliable has to await more and highly accurate data in this regime (e.g., Battaglia et al. 2008). Nonetheless, the CaT index is well suited to the identification of candidates for fairly metal-poor stars, although the exact  $[\text{Fe}/\text{H}]$  value may not be measurable – this is then left for follow-up high-resolution studies.

#### 4.2. Alpha Elements – O, Mg, Si, Ca, Ti

While iron is synthesized both in SNe II and SNe Ia, the even- $Z$  elements (O, Mg, Si, Ca, Ti) are predicted to be produced during (nucleosynthetic) shell-burning in high-mass stars with very short lifetimes, which later end their lives in SN II explosions.

A simple scenario for the formation of the Galactic halo is that an initial burst of SF produces large amounts of  $\alpha$ -elements on short time scales, leading to an enhanced  $[\alpha/\text{Fe}]$  ratio. At these early epochs, the long-lived SNe Ia did not yet have time to significantly pollute the initial SNe II abundance pattern. Once SNe Ia start to contribute (after a delay of  $\sim 1$  Gyr from the onset of SF), iron production will increase, leading to a decline in the  $[\alpha/\text{Fe}]$  abundance ratio. As noted above, the detailed patterns of the transitions in  $[\alpha/\text{Fe}]$  with metallicity (taken as a proxy for time) are dependent on the specific SF history of a stellar system, on its stellar IMF, and on the timescales for mixing the SNe products into the interstellar medium (ISM) (Matteucci 2003; S03; Venn et al. 2004).

The metal-poor stars of the Galactic halo evidently populate a plateau of  $[\alpha/\text{Fe}] \sim 0.4$  dex (see, e.g., the review by McWilliam 1997). From the available analyses of 36 red giants in seven dwarf galaxies, S03 found at best little evidence to identify these stellar populations with those in the Milky Way. In fact, stars in dSphs have been shown to be quite different from Galactic disk, and even more so from halo stars, in that they have lower  $[\alpha/\text{Fe}]$  ratios (e.g., Shetrone et al. 2001; Pritzl et al. 2005; see also Fig. 3). Hence, these elements have often been considered as an important test for Searle & Zinn’s (1978) hypothesis of the origin of the Galactic halo from satellite accretion events (Unavane, Wyse and Gilmore 1996).

Despite the characteristic relatively low  $[\alpha/\text{Fe}]$  in most stars of the dSphs, their wide abundance range from approximately  $-3.0$  to  $0.3$  dex and the fact that some stars also exhibit higher, Galactic  $[\alpha/\text{Fe}]$  values suggests that using these elements as a test for chemical imprints of accretion events requires a sophisticated analysis (Venn et al.

2004). Irrespective of this analysis, the  $\alpha$  elements provide important information in elucidating the evolutionary histories of individual dwarf galaxies (e.g., S03; T03). We will turn to discussing the implications of our derived  $[\alpha/\text{Fe}]$  ratios for Carina’s chemical evolution in Section 5.

Figs. 2 through 4 display the derived abundances for each  $\alpha$ -element in our Carina stars, together with the measurements of five red giants in Carina of S03, where none of their targets coincides with our present sample. The  $\alpha$ -elements are displayed individually as well as a combination of these elements as the parameter  $[\alpha/\text{Fe}] = [(\text{Mg} + \text{Ca} + \text{Ti})/3\text{Fe}]$  (see also Table 1 in Venn et al. 2004). The right panels of Fig. 2 and Figs. 3, 4 also include a compilation of Galactic thin and thick disk stars as well as a large number of halo field stars<sup>16</sup>. Note that the separation into Galactic components is purely based on kinematic information.

In order to compare Carina’s elemental abundances with those of stars in other Local Group galaxies, we show also currently available abundance ratios for stars in eight Galactic dSphs (Draco, Sextans, UrsaMinor from Shetrone et al. 2001; Sculptor, Fornax, Leo I, Carina from S03; UrsaMinor from Sadakane et al. 2004; Sculptor from Geisler et al. 2005 and Sagittarius from Monaco et al. 2005).

When comparing data sets from various sources, as was done by Venn et al. (2004) and as is shown in Figs. 3 and 4 here, one has to keep in mind that each analysis may use different spectral lines, presumably differing oscillator strengths, and different model atmosphere techniques. The combination of such data will then result in an analysis-dependent spread in the abundance ratios, which is of the order of 0.1–0.2 dex (Venn et al. 2004), a value comparable to the abundance offsets found by S03 by using different stellar atmospheres and atomic data. In the light of our measurement uncertainties (Sect. 3.3; indicated by the error bars in the figures), we did not attempt to homogenize the data shown in the subsequent Figures. This measurement method induced scatter does not alter any of the conclusions we draw below.

The first thing to note is that one of our target stars, LG04a\_001826, exhibits a strong depletion in almost all of the  $\alpha$ -elements, although it is moderately metal rich, at  $[\text{Fe}/\text{H}] = -1.49$  dex. This star will be discussed further below.

As Venn et al. (2004) note, the scatter in  $[\text{Mg}/\text{Fe}]$  is expected to be much larger than that in either  $[\text{Ca}/\text{Fe}]$  or  $[\text{Ti}/\text{Fe}]$ , an expectation which is met by our data. Apart from the strongly discrepant target at  $[\text{Fe}/\text{H}] = -1.49$ , with  $[\text{Mg}/\text{Fe}] = -0.92$ , the more metal rich targets cover a full range in  $[\text{Mg}/\text{Fe}]$  from  $-0.24$  to  $+0.08$  dex, while the two most metal-poor stars in our sample exhibit enhanced Mg abundances of 0.3 and 0.4 dex, and thus partially overlap with the Galactic halo. In order to test the extent to which the scatter can be considered intrinsic, we compared the observed scatter in the abundance ratios to the value predicted from a set of Monte Carlo simulations, in which our measurements were varied by the observational uncertainties. While the predicted and observed  $1\sigma$ -scatter are similar for the cases of  $[\text{Ca}/\text{Fe}]$  and  $[\text{Ti}/\text{Fe}]$ , the observed scatter in  $[\text{Mg}/\text{Fe}]$ , at 0.16 dex, exceeds that expected from

<sup>16</sup> The stellar abundances for these illustrations are tabulated in Venn et al. (2004), who in turn assembled the data from various literature sources. See their paper for references.



the pure observational uncertainties by  $\sim 0.05$  dex, indicating a real dispersion.

Ca is predominately produced in intermediate-mass progenitor SNe II (Woosley & Weaver 1995). While the most metal-poor stars of the Shetrone et al. (2001) and S03 samples in Sextans and Draco are clearly depleted w.r.t. the Galactic components (at  $[\text{Ca}/\text{Fe}] \sim 0.1$ ), our most metal-poor Carina giant is significantly enhanced in Ca (by 0.7 dex). However, already the second most metal-poor star (0.2 dex more metal rich) has a  $[\text{Ca}/\text{Fe}]$  that is only slightly larger than the average we find from the rest of our sample ( $\langle [\text{Ca}/\text{Fe}] \rangle = 0.09 \pm 0.14$  dex). While the majority of our targets with  $[\text{Fe}/\text{H}] > -2$  tend to follow the trend of the other dSphs' Ca abundances, and also are consistent with S03's measurements, one should note that three or four of the more metal-rich giants have comparable enhancements to those of the Galactic thick disk and/or halo.

Although it is still unclear if the nucleosynthesis of Ti proceeds in analogy to the other  $\alpha$ -elements (e.g., Timmes et al. 1995; Woosley & Weaver 1995), it is traditionally included in the group of these elements due to its similarly enhanced abundances in metal-poor stars (Gratton & Snenen 1991). With the exception of the strongly depleted LG04a\_001826, Ti in Carina tends to follow the overall trends of the other  $\alpha$ -elements, with an average abundance significantly lower than the Galactic halo star abundance ratios. In fact, the two most metal-poor stars of our sample show enhanced  $[\text{Ti}/\text{Fe}]$  of  $\sim 0.1$  and 0.36 dex, which is consistent with the Galactic halo, but at odds with the two comparably metal-poor red giants from Shetrone et al. (2001) and S03. The latter stars, in the Sextans and Draco dSphs, are deficient in  $[\text{Ti}/\text{Fe}]$  by  $\sim -0.23$  dex. The majority of our targets is consistent with both the Carina data and most of the other dSphs' abundances of Shetrone et al. (2001) and S03.

Si is often considered a prototypical  $\alpha$ -element. Its production site is identified with SNe II of moderate progenitor masses, around  $20 M_{\odot}$  (Woosley & Weaver 1995). In our data we were able to determine its abundance from typically three lines. For the most metal-poor star no information could be extracted, since no measurable line was detected in its spectrum.

In the second most metal-poor star, there is a strong indication of a significant enrichment in Si, as found in most metal-poor stellar abundance studies (McWilliam 1997; Prochaska et al. 2000; Venn et al. 2004, and references therein). As Fig. 4 implies, an enhancement of  $\sim 0.9$  dex is not atypical for metal-poor giants in dSphs and also is found in UMi (Shetrone et al. 2001). Our stars show a lower average  $[\text{Si}/\text{Fe}]$  compared to the Shetrone samples, where our mean value is  $\langle [\text{Si}/\text{Fe}] \rangle = -0.01 \pm 0.12$  dex (for  $[\text{Fe}/\text{H}] > -2$ ). It is worth noticing, however, that there is a fair amount of scatter in  $[\text{Si}/\text{Fe}]$ , both in the Galactic halo and all dSph samples considered here, including our own data. In this context,  $[\text{Si}/\text{Fe}]$  abundance ratios as low as  $-0.4$  are also found in other dSphs of the Local Group. While the second most metal poor star is enhanced in  $[\text{Si}/\text{Fe}]$ , the abundance ratios around Carina's mean  $[\text{Fe}/\text{H}]$  typically reach from about  $-0.2$  up to  $+0.15$  dex in our targets. Owing to the overall scatter, some of the dSphs' stellar abundances overlap with the Galactic halo component at  $[\text{Si}/\text{Fe}] \sim +0.4$ .

Oxygen abundances were measured from the two forbidden lines at  $\lambda\lambda 6300, 6363 \text{ \AA}$ , which are, however, not detectable in the most metal poor target, nor in the overall depleted star of LG04a\_001826. We find a range in  $[\text{O}/\text{Fe}]$  from  $-0.2$  to  $+0.65$  dex with a considerable star-to-star scatter at a given  $[\text{Fe}/\text{H}]$  (Fig. 5, top panels). As Fig. 5 (bottom) implies, the range in  $[\text{O}/\text{Fe}]$  in Carina, as well as the increased scatter compared to the other  $\alpha$ -elements, is consistent with that found in other dSphs. As mentioned above, these abundances are depleted w.r.t. the Galactic halo by  $\sim 0.5$  dex and show a well defined decline with  $[\text{Fe}/\text{H}]$  at lower metallicities than in the Galaxy.

#### 4.3. Sodium

Sodium abundances were determined from the absorption lines at  $5682$  and  $5688 \text{ \AA}$ . We did not include hyperfine splitting in the calculations, since its effect is expected to be negligible (McWilliam et al. 1995). As Fig. 5 (bottom panels) implies, our mean  $[\text{Na}/\text{Fe}]$  in Carina of  $-0.36$  dex with its scatter of  $\sim 0.27$  dex is consistent with the Carina values of S03, and also with the  $[\text{Na}/\text{Fe}]$  in the other dSphs. In particular, there is a strong overlap of Carina's Na abundance with the Galactic halo stars, which also cover a broad range.

It is worth noticing that there is no trend of  $[\text{Na}/\text{Fe}]$  with oxygen discernible. Such a pattern would be evidence of deep mixing. In deep mixing, processed material from the interior of a star can be transported into the upper atmosphere. Nucleosynthetic burning converts O, N and Ne to Na, whereas Mg is converted into Al in the deeper atmospheric layers of red giants. Hence, typical deep mixing patterns predict that an atmospheric depletion in O coincides with an enhancement of Na (Langer et al. 1993), while any observed Mg depletion is accompanied by an enhanced Al abundance (Langer & Hoffmann 1995). Unfortunately, in none of our spectra could Al be detected, since all suitable lines in our spectral range are too weak. Interestingly, such (anti-) correlations are detected in globular clusters both in the Galaxy (Pritzl et al. 2005 and references therein) and in dSphs (Letarte et al. 2006), but they are not observed in Galactic field stars (Gratton et al. 2004) nor in dSph field stars (S03; Venn et al. 2004). Consistent with this, our Carina red giants show a constant mean  $[\text{Na}/\text{O}]$  of  $\sim -0.63 \pm 0.17$  over the full range of metallicities.

#### 4.4. The $\alpha$ -depleted case of LG04a\_001826

We now turn to the question of whether our target star LG04a\_001826, which shows a considerable depletion in almost all of the  $\alpha$ -element ratios, i.e., in  $[\text{Mg}/\text{Fe}]$ ,  $[\text{Ca}/\text{Fe}]$  and  $[\text{Ti}/\text{Fe}]$ , can provide further insight into general galactic evolution or whether it should rather be considered a special case. For this star  $[\text{Mg}/\text{Fe}]$  lies  $2.2\sigma$  below the sample average, and  $[\text{Ca}/\text{Fe}]$  and  $[\text{Ti}/\text{Fe}]$  are underabundant by  $1.8\sigma$  and  $2.3\sigma$ , respectively, w.r.t. the mean abundance ratios in Carina.

One possible interpretation of a selective depletion of the  $\alpha$ -elements could be the occurrence of deep mixing, but as discussed above, this is not seen in other stars in dSphs. Moreover, at  $[\text{Na}/\text{Fe}] = -0.48$  LG04a\_001826 shows a sodium abundance that is consistent with the mean  $[\text{Na}/\text{Fe}]$  ratio found from all our Carina stars, and Na

is not overly enhanced w.r.t. the non-detection of oxygen in its photosphere. It appears unlikely that this star's abundance patterns are influenced by deep mixing. An untestable hypothesis is that enrichment by rapidly rotating massive stars may be involved, since this can lead to globular-cluster-like abundance anomalies, dredging-up processed material into the outer layers of the massive stars, where it may be lost as a wind prior to the Type II supernova (Decressin et al. 2007).

Generally speaking, the  $\alpha$ -elements are synthesized in core-collapse SNe II, where different elements originate in different stages of these endphases in the lives of massive stars. Oxygen and magnesium, which show the strongest depletion (Mg) or upper limits (O) in this star, are produced mainly during the hydrostatic burning phases. Their yields are primarily a function of the progenitor's mass, but are heavily affected by the thickness of the burning shells, the treatment of rotation and convection, and the mass cut between the proto-neutron star and the SN ejecta (Thielemann et al. 1996; Argast et al. 2002). If one assumes a larger range of possible realizations of these factors, a larger scatter in the resulting element ratios such as [O/Fe] and [Mg/Fe] is feasible (Argast et al. 2002; Venn et al. 2004). Depending on the exact mass of the SN II progenitor, a low value of [Mg/Fe] is possible (see Fig. 1 in Argast et al. 2002). Low [Mg/Fe] is observed in a few metal poor bulge-stars (McWilliam et al. 1995) and in mildly metal-poor halo stars (e.g., Carney et al. 1997; Ivans et al. 2003).

Some SN models (like those of Argast et al. 2000, 2002) predict the occurrence of such depleted stars at lower, halo-like metallicities, specifically due to the mixing of SN ejecta into a gas reservoir of  $\sim 10^4 M_{\odot}$ . Comparable variations at a higher [Fe/H], as seen in the case of LG04a.001826, can be explained analogously with reasonable parameters, particularly noting the uncertainties associated with the modelling of Mg and Fe yields. Alternatively, one could assume that our target star exhibits a normal average abundance of Mg, but has an anomalous Fe abundance. Then its low [Mg/H] would be representative of a halo-like star of [Fe/H]  $\sim -2.6$  dex. In this case, in order to realize its comparatively low [Mg/Fe], LG04a.001826 had to originate from SNe Ia pre-enriched material (Gilmore & Wyse 1998). This would be diluted less than the characteristic halo ISM or could be subject to a significantly higher iron yield, producing a [Fe/H] higher by  $\sim 1.1$  dex than expected from its  $\alpha$ -yield.

The other  $\alpha$ -elements Si, Ca and Ti originate in explosive burning during the SN event itself and depend primarily on the explosion energy and to a lesser extent on the amount of material available to be burned and the binding energy of the star, that is, its mass (e.g., Woosley & Weaver 1995). Since typical explosion energies cover only a small range, the abundance ratios of these elements can be expected to show a much lesser scatter, which is in fact in agreement with the observations (Venn et al. 2004; see also Figs. 3 and 4).

It is then odd that this star exhibits a rather average [Si/Fe] ratio (at  $0.2\sigma$  below the sample mean). It has been suggested that Si contains a non-negligible admixture of material originating in hydrostatic burning (Timmes et al. 1995; Thielemann et al. 1996; Argast et al. 2000) and it

is then likely that the resulting abundance patterns can differ from a pure explosive origin as for Ca or Ti (but see Cohen et al. 2007 for the exact opposite pattern).

The intermediate-mass  $\alpha$ -element Ti has also a contribution from complete Si burning with an  $\alpha$ -rich freeze-out (Thielemann et al. 1996 and references therein). Differences between Ca, Si, and Ti are thus naturally to be expected. Finally, the production of Ti is not yet fully understood (Woosley 1986; Woosley & Weaver 1995) and Galactic evolution models often fail to reproduce the observed abundance patterns (e.g., Timmes et al. 1995). A detailed interpretation of this star's abundance ratios in terms of the yields for each individual  $\alpha$ -element has to rely on fine-tuned nucleosynthetic modeling and is presently hampered by the lack of an accurate understanding of the exact SN II explosion mechanism (e.g., see discussions in Woosley & Weaver 1995; Timmes et al. 1995; McWilliam et al. 1995; Thielemann et al. 1996; Argast et al. 2000, 2002).

All in all, the presence of a strongly  $\alpha$ -element depleted object would seem to suggest that we see here the influence of *single* SN events. Contrary to a homogeneous, close-to-uniform [ $\alpha$ /Fe] pattern resulting from well-mixed, IMF-averaged SNe, this star is likely to reflect the imprint of stochastic inhomogeneous chemical evolution, where the star formed from unmixed SN ejecta. Rather than (over-) interpreting this star's abundance pattern in terms of Carina's SF history we attribute it to statistical fluctuations due to incomplete ISM mixing. That such incomplete mixing may occur also in actively star-forming dwarf galaxies was recently shown by Kniazev et al. (2005). It is then also possible to assign the strong Ca enhancement of the most metal-poor star in our sample to such scatter, which becomes progressively dominant in metal-poor stars of [Fe/H]  $\lesssim -3$  dex. This contrasts with the low scatter in the more metal poor Galactic halo, indicative of a well-mixed ISM even at very early times (e.g., Cayrel et al. 2004; François et al. 2004). Of course, any distinction between Carina and the halo based on the small number of peculiar stars in Carina should be taken with caution: while the dispersion in the abundance ratios of metal poor halo stars is in fact smaller than would be expected if *all* metal poor stars were polluted by single SNe, there are a number of chemically peculiar metal poor stars present in the halo (e.g., Norris et al. 2002; Cohen et al. 2007).

Fortunately, observational analyses of  $\alpha$ -depleted stars in the Galactic halo are underway, and will quantify how SNe Ia and SNe II contribute to their abundance patterns. For instance, Ivans et al. (2003; and references therein) investigate three moderately metal poor halo stars ([Fe/H]  $\sim -2$ ) with unusually low  $\alpha$ - and neutron capture element abundances. By comparison with the abundance patterns of very metal poor stars, these stars were argued to be iron rich rather than  $\alpha$ -poor. As in our Carina case, their depletion in [ $\alpha$ /Fe] would be explicable in terms of a contribution of SNe Ia yields that is larger than expected given their low metallicities. It is conceivable that such stars may have been born out of material that was polluted by the earliest SNe Ia to have occurred in the Milky Way (Nissen & Schuster 1997; Ivans et al. 2003). It has been suggested that at least a fraction of this new class of Galactic halo stars may have been captured from ac-

creted, dSph-like systems. Despite the general discrepancy between the halo and present-day dSph abundances, our finding of such a peculiar,  $\alpha$ -depleted star in Carina then makes feasible a partial accretion origin of this chemically distinct halo subpopulation.

##### 5. IMPLICATIONS FOR CARINA'S CHEMICAL EVOLUTION

Apart from the two most metal-poor stars in our sample and the strongly depleted red giant LG04a.001826, the majority of our targets are compatible with solar  $\alpha$ -abundances: we find a mean  $[\alpha/\text{Fe}]$  of  $0.00 \pm 0.10$  dex. Our data confirm the earlier important finding that the  $\alpha$ -elements in dSph stars are significantly depleted w.r.t. Galactic halo stars of the same metallicity (Shetrone et al. 2001; S03; T03; Venn et al. 2004). It is interesting to note that the two most metal-poor stars in Carina show an enhancement in the  $\alpha$ -elements by  $\sim 0.3$  and  $0.4$  dex, which is the same order of magnitude as seen in the halo stars. These stars should then also be expected to be the oldest stars to have formed and may have been born at an *early* epoch, when SNe Ia had not yet started to contribute, but when an initial starburst had already polluted the pristine material with a significant amount of the  $\alpha$ -elements ejected in short-lived SNe II. In general, dSph stars populating the same SNe II plateau as the Galactic halo are consistent with an invariant, massive star, IMF (e.g., Wyse et al. 2002).

On the other hand, those stars with higher metallicities (between  $\sim -1.8$  and  $-1.3$  dex) resemble stars in other dSph galaxies. These progressively lower values of  $[\alpha/\text{Fe}]$  are characteristic of the slow chemical evolution and low SF rates in dwarf galaxies (Unavane et al. 1996; Matteucci 2003). Differences between individual galaxies' abundance ratios are, of course, to be expected, since these chemical tracers sensitively depend on the details of each galaxy's environment, SF history, IMF, etc. Overall, our stars' abundance ratios are also in good agreement with the values found in the five stars studied by S03.

It has been proposed that Carina's episodic SF history, i.e., its sequence of bursty and quiescent phases, is reflected in the  $[\alpha/\text{Fe}]$  abundance ratios (S03, T03). S03 suggested that the considerable rise in  $[\alpha/\text{Fe}]$  – after the typical decline due to the continuing feedback from SNe Ia – seen in their data at  $[\text{Fe}/\text{H}] \sim -1.65$  indicates that these stars may be related to either Carina's second SF episode around 7 Gyr ago or to an intermediate SF event well before this episode. Both interpretations are compatible with photometric determinations of Carina's SF history and the times of each SF episode and hiatus (Smecker-Hane et al. 1996; Hurley-Keller et al. 1998; Rizzi et al. 2003). Any connection is strengthened by comparable variations in a number of heavy element abundance ratios. Resolving and quantifying the SF history clearly requires further investigation: the interpretation of S03 and T03 was based on only 5 stars with limited age resolution.

We combine our data for the  $\alpha$ -elements O, Mg, Si and Ca with the measurements from S03. The resulting data set represents the entire currently available high-resolution abundance data for Carina (we do have a larger study underway). It is tempting to interpret the  $[\alpha/\text{Fe}]$  pattern of the full data set (Figs. 3 and 6) in terms of Carina's episodic SF. S03 have noted a rise in  $[\alpha/\text{Fe}]$  between  $-1.65$

and  $-1.6$  dex from their 5 stars. This rise is also discernible in the full data set including S03's and our ten stars, where it is most distinct in  $[\text{O}/\text{Fe}]$  and less pronounced in the other elements. After a decline in SF rates, the  $[\alpha/\text{Fe}]$  ratio may rise again towards a maximum at around  $[\text{Fe}/\text{H}] = -1.4$  dex, before leveling off again. However, in the light of the measurement uncertainties (see also Fig. 6, bottom right) the run of  $[\alpha/\text{Fe}]$  vs.  $[\text{Fe}/\text{H}]$  for most of our stars (disregarding the most metal-poor and strongly  $\alpha$ -depleted star for the moment) and those of S03 can equally well be considered to be constant (see bottom right panel of Fig. 6), with some, perhaps intrinsic, scatter in  $[\alpha/\text{Fe}]$ . Uniformly low  $[\alpha/\text{Fe}]$  ratios over a wide range of metallicities would then point to the fact that Carina's SF was in fact dominated by SNe II driven blow-out (e.g., Mac Low & Ferrara 1999; Paper I).

In Fig. 7, we compare the full observational set with the models from Lanfranchi et al. (2006, hereafter LMC06), which are an extension of the models presented in Lanfranchi & Matteucci (2004). This set of models was tailored, modifying best-fit SF and wind efficiencies, so as to reproduce the total mass, present-day gas mass and the few elemental abundances available at that time for a number of dSphs. In addition to the aforementioned observables used in Lanfranchi & Matteucci (2004), LMC06 also incorporated our MDF of Carina from Paper I to update their choice of model parameters. A marginally higher SF efficiency (of  $0.15 \text{ Gyr}^{-1}$ ) and a slightly lower wind efficiency (of 5 times the SF rate) were adopted to better match our observations. The models described in Lanfranchi & Matteucci (2004) assumed Carina's SF history according to Hernandez, Gilmore, & Valls-Gabaud (2000), and so are lacking a significant very old population, (e.g., Smecker-Hane et al. 1994; Harbeck et al. 2001; Monelli et al. 2003; Grebel & Gallagher 2004). The LMC06 models adopt the SF history from Rizzi et al. (2003). In this latter study, the SF was found to have occurred episodically with an initial active period at an early epoch, while the majority of stars were formed  $\sim 3\text{--}7$  Gyr ago.

For all the elements shown in Fig. 7 there is a sudden decrease in the computed  $[\alpha/\text{Fe}]$  at  $[\text{Fe}/\text{H}] \sim -1.6$ , consistent with a combination of the onset of galactic winds and the injection of Fe into the ISM via SN Ia events. Once the winds set in, the available amount of gas for SF is reduced, resulting in a decline of the overall SF. Consequently, the formation of new stars almost ceases and, in turn, the occurrence of SNe II and the related production and injection of the  $\alpha$ -elements is halted as well. Since Fe is continuously produced and injected into the ISM by the longer timescale SNe Ia for several Gyr, unaffected by cessation of SF, the start of efficient winds leads to the sudden decrease seen in the modeled  $[\alpha/\text{Fe}]$  abundance ratios. It is, however, not obvious *a priori* that the SF rate and thus the associated SNe II rate was high enough to sustain winds – these free parameters are put in by hand in the LMC06 models.

For Ca the majority of our stars lie above the models, while the observed  $[\text{Mg}/\text{Fe}]$  and  $[\text{Si}/\text{Fe}]$  ratios tend to lie below the predictions at any given metallicity. This may in part be attributed to the large scatter in  $[\alpha/\text{Fe}]$  for basically all metallicities, a scatter which also has been reported to exist in previous observational studies (see Pritzl

et al. 2005 and references therein). At present, the models appear to provide at best an upper limit to the observations, given the overall large star to star scatter, and thus reproduce the more chemically enhanced stars reasonably well. One should keep in mind that the original model parameters were optimized to fit the abundance patterns as observed by S03 so that the overall trends in their element ratios are fit fairly well.

The overall impression to glean from Fig. 7 is that, in spite of being able to predict certain patterns in chemical abundance ratios, there is a general need for models of chemical evolution to steadily improve the parameters governing the SF processes. In essence, matching the full sample of available  $\alpha$ -elemental data appears to require a turnoff from the plateau in  $[\alpha/\text{Fe}]$  at *lower* metallicities (again with the exception of Ca). These low abundances at higher metallicities may be achieved by adopting a less intense wind and/or a cessation in SF at earlier epochs. More intense winds would provide lower values for *all*  $[\alpha/\text{Fe}]$  ratios, once the wind developed, due to the correspondingly decreased SF rate. Limitations can be attributed to the difficulties in assuming a specific SF history for the models and will depend both on the number, duration, and times of the assigned SF episodes. Similarly, an overall lower SF efficiency would be able to retain the lower  $[\alpha/\text{Fe}]$  values. Since these parameters affect the shape of Carina’s MDF (recall that they have been adjusted to match the latter) it is clear that ideally the MDF, the full set of observed abundance ratios and a fully sampled SF history have to be simultaneously taken into account in order to reliably devise the evolutionary history of Carina. Considering the discussion in Sect. 4.4, it is also conceivable that stochastic SF, e.g., in small associations, and inhomogeneous enrichment, may have played a major role in Carina’s history.

In Fig. 8 we overplot a set of chemical evolution models from Gilmore & Wyse (1991) with our observed oxygen abundance ratios. In these models, which were the first chemical evolution models to account naturally for below-solar  $\alpha$ -element ratios at low metallicities, SF occurs in an initial, short-lived burst, during which there is no significant contribution from SNeIa. This active period is followed by a quiescent phase lasting several Gyr, during which only SNeIa enrich the ISM. A second, late SF burst is assumed to set in at higher metallicities. In the figure, the first burst occurs at  $[\text{Fe}/\text{H}] = -2.1$  dex, while the second SF sets in at  $-1.1$  (solid line) and  $-1.4$  dex (dashed line). We did not aim at optimizing the exact onset of each burst to constrain Carina’s SF history, but rather shifted the predictions of Gilmore & Wyse (1991), which were originally computed to represent the chemical evolution of the LMC and SMC. It is then intriguing that already this simple scenario yields an amazingly good representation of our data, and that the observed increase and scatter in the abundance patterns can in fact be assigned to an increase in SF activity, perhaps associated with separate SF episodes 7 and 3 Gyr ago (Hurley-Keller et al. 1998). This comparison indicates that the onset of the second epoch of SF has to be around an abundance of  $-1.5$  dex. It cannot be ruled out by our data that two SF bursts have occurred in the interval between  $\sim -2$  and  $\sim -1.4$  dex, which is probable given the fact that deep photo-

metric studies agree on the occurrence of three major SF episodes in Carina (Smecker-Hane et al. 1996).

The occurrence of SF bursts should cause variations in both  $[\text{O}/\text{Fe}]$  and the other  $\alpha$ -elements, whereas the observed scatter in  $[\text{Ca}/\text{Fe}]$  and  $[\text{Ti}/\text{Fe}]$  is smaller than that seen in our  $[\text{O}/\text{Fe}]$  abundance ratios. As Gilmore & Wyse (1991) argue, inhomogeneities in the location and onset of each SF burst inevitably leads to a large scatter in the abundance ratios, such as seen in Carina. Even in the presence of a statistically universal IMF, the intrinsically rare high-mass stars will form with significant random number fluctuations in SF events of small total mass: SF events that produce only a small total mass in stars might not form any of the highest-mass oxygen-producing stars at all. Adopting a standard IMF (e.g., Miller & Scalo 1979), it can be shown that  $M_{\text{tot}} \sim 100M_{\odot}$  form in low-mass stars per SN II ( $M \geq 10M_{\odot}$ ), while  $\sim 4000M_{\odot}$  form in the lower-mass regime of the IMF for every  $40M_{\odot}$  star. Thus, in a system like Carina, where SF involves small numbers, as well as low rates, the resulting mass-averaged IMF yield will have inevitable stochastic scatter, contributing to observed intrinsic scatter in our abundance ratios. Effective truncation of the massive-star IMF due to a low SF rate was suggested by T03 as a mechanism to produce low values of  $[\alpha/\text{Fe}]$  in dSph stars, treating the entire galaxy as a “single-cell star-forming entity”. Our model comparison and the new, more numerous data allow us here to identify additional new key elements – inhomogeneous, stochastic SF in low-mass associations or clusters, with incomplete mixing leading to inhomogeneous chemical evolution. Overall, our data suggest that Carina’s evolution involved non-monotonic, stochastic, low-rate SF that forms marginally bound low-mass stellar associations and/or clusters, convolved with incomplete mixing of the SNe ejecta into the ISM.

## 6. CONCLUSIONS

We have derived elemental abundance ratios for a number of light chemical elements in ten red giants in the Carina dSph, tripling the existing sample for this galaxy. By adding these ten stars to the presently existing data for  $\sim 50$  red giants in eight out of the 17 currently known dSph satellites of the MW system, the sparse chemical information available for dSph galaxies slowly continues to grow, confirming the overall trends in element abundance ratios noticed in earlier studies.

As a number of our stars were also observed at lower resolution, we could compare metallicity estimates from the well established *calcium* triplet (CaT) calibration with the high-quality *iron* abundances from the present work. We show that the CaT-based metallicities and the true iron abundances agree remarkably well in the relatively metal-rich regime of  $[\text{Fe}/\text{H}] \gtrsim -2$  dex. For the single more metal-poor star overlapping with the high-resolution sample we find a substantial difference in the metallicity derived from the CaT and high-resolution iron lines. This may be since the CaT calibration needs to be extrapolated below  $[\text{Fe}/\text{H}] \lesssim -2$  dex. Since we have only one data point, a more complete sampling of the dSphs’ metal-poor stars with high-resolution spectroscopy is desirable. The red giants in Carina span a comparable range in  $[\text{Ca}/\text{Fe}]$  to the GGCs that we used to calibrate Carina’s low-resolution

MDF in Paper I, so we argue that the application of the CaT method to devise a global metallicity is valid within the range of the calibration.

The majority of the elements observed follow the patterns seen in other MW satellite dSphs (S03; Venn et al. 2004), i.e., they lie generally below the Galactic halo star values. This is consistent with low SF efficiency governing the internal evolution of the dwarfs, but is not consistent with halo formation by accretion of present-day satellites (Shetrone et al. 2001). Our Mg abundances show larger scatter than do Ca and Si, as anticipated by their different nucleosynthetic formation processes.

We detect two metal-poor objects at  $-2.5$  and  $-2.7$  dex. These are significantly  $\alpha$ -enhanced and exhibit halo-like abundance ratios, while the most metal-poor star is even more strongly enhanced in Ca. Overall, it appears that the Ca ratios are slightly higher on average than the remainder of the  $\alpha$ -elements. Therefore the relatively metal poor stars in the Galactic halo can in fact be considered as remnants from an accreted dSph satellite, if this merger event occurred very early on (e.g., Grebel et al. 2003; Carollo et al. 2003).

Our sample hosts one star that is remarkably depleted in almost all elements. Possible explanations include a particularly high iron yield or the imprint of single SN events, the latter of which points to the presence of early stochastic fluctuations and an incomplete mixing of the ISM gas. This may indicate that SF in Carina occurred stochastically within smaller constituents, followed by an inhomogeneous enrichment of the surrounding medium. If SF in dissolving star clusters was a major contributor in Carina, one might be able to identify the clusters' remnants. Chemical substructure is, however, generally not observed in the low mass dwarf galaxies (but see Kleyna et al. 2003), nor in transition-type galaxies. Localized evidence of abundance inhomogeneities on small scales at a given time, which argues in favor of SF in *associations*, has been detected in a few dwarf irregular galaxies (e.g.,

Grebel & Richtler 1992; Gonzalez & Wallerstein 1999; Kniazhev et al. 2005).

We compare our data to models that include several bursts in Carina's SF history and conclude that the anticipated low SF efficiencies and moderate mass-loss rates in dSphs provide reasonable representations of present-day data sets, although they fail to produce the observed abundance scatter. There are still deficiencies in the detailed models concerning some single elements. In particular the Ca measurements are at odds with the models, having systematically higher abundances on average. We note that the LMC06 models that we compared to our data did not account for incomplete mixing, which we, however, observe. By adopting a model prediction with two SF bursts and an extended hiatus, which is qualitatively justified by Carina's SF history from its CMD, we argue that the second burst in Carina must have occurred at an approximate  $[\text{Fe}/\text{H}]$  of  $-1.5$ . This burst metallicity is not quantitatively constrained by CMDs, and hence is a prediction for future abundance measurements (see also S03). Such predictions become testable, once metallicities and robust age estimates of stars on the subgiant branches of Carina are available. Although our data do not rule out any imprints of Carina's episodic SF, we did not attempt to quantify the underlying exact SF history, which is further impeded by the lack of accurate age information for our target stars.

A.K. and E.K.G. are grateful for support by the Swiss National Science Foundation (grants 200020-105260; 200020-113697). M.I.W. acknowledges the Particle Physics and Astronomy Research Council for financial support.

We would like to thank A. McWilliam for providing his versions of the atmosphere interpolators and photometric gravity codes and helpful discussions. F.-K. Thielemann and G. Lanfranchi are acknowledged for helpful comments.

## REFERENCES

- Akerman, C. J., Carigi, L., Nissen, P. E., Pettini, M., & Asplund, M. 2004, *A&A*, 414, 931
- Alonso, A., Arribas, S., & Martínez-Roger, C. 2001, *AJ*, 376, 1039
- Anders, E., & Grevesse, N. 1989, *Geochim. Cosmochim. Acta*, 53, 197
- Argast, D., Samland, M., Gerhard, O. E., & Thielemann, F.-K. 2000, *A&A*, 356, 873
- Argast, D., Samland, M., Thielemann, F.-K., & Gerhard, O. E. 2002, *A&A*, 388, 842
- Armandroff, T.E., & Da Costa, G.S. 1991, *AJ*, 101, 1329
- Asplund, M., Grevesse, N., & Sauval, A. J. 2005, in *ASP Conf. Ser., Cosmic Abundances as Records of Stellar Evolution and Nucleosynthesis*, ed. T.G. Barnes III & F.N. Bash (San Francisco: ASP), 236, 25
- Bai, G. S., Zhao, G., Chen, Y. Q., Shi, J. R., Klochkova, V. G., Panchuk, V. E., Qiu, H. M., & Zhang, H. W. 2004, *A&A*, 425, 671
- Bard, A., & Kock, M. 1994, *A&A*, 282, 1014
- Battaglia, G., Irwin, M., Tolstoy, E., Hill, V., Helmi, A., Letarte, B., & Jablonka, P. 2008, *MNRAS*, 383, 183
- Bessel, M. S. & Brett, J. M. 1988, *PASP*, 100, 1134
- Blackwell, D. E., Smith, G., & Lynas-Gray, A. E. 1995, *A&A*, 303, 575
- Boesgaard, A. M., King, J. R., Deliyannis, C. P., & Vogt, S. S. 1999, *AJ*, 117, 492
- Bosler, T. L., Smecker-Hane, T. A., & Stetson, P. B. 2007, *MNRAS*, 378, 318
- Cardelli, J. A., Clayton, G. C., & Mathis, J. S. 1989, *ApJ*, 345, 245
- Carney, B. 1996, *PASP*, 108, 90
- Carney, B. W., Wright, J. S., Sneden, C., Laird, J. B., Aguilar, L. A., & Latham, D. W. 1997, *AJ*, 114, 363
- Carollo, D., et al. 2007, *Nature*, 450, 1020
- Carrera, R., Gallart, C., Pancino, E., & Zinn, R. 2007, *AJ*, 134, 1298
- Carretta, E., & Gratton, R. 1997, *A&AS*, 121, 95
- Carretta, E. 2006, *AJ*, 131, 1766
- Castelli, F., & Kurucz, R. L. 2003, in *IAU Symp. 210, Modelling of Stellar Atmospheres*, eds. N.E. Piskunov, W.W. Weiss, & D.F. Gray (San Francisco: ASP), A20 (astro-ph/0405087)
- Cayrel, R., et al. 2004, *A&A*, 416, 1117
- Cohen, J. G., & Meléndez, J. 2005, *AJ*, 129, 303
- Cohen, J. G., McWilliam, A., Christlieb, N., Shtetman, S., Thompson, I., Melendez, J., Wisotzki, L., & Reimers, D. 2007, *ApJ*, 659, L161
- Cutri, R. M. 2003, Explanatory Supplement to the 2MASS All-Sky Data Release, <http://www.ipac.caltech.edu/2mass/releases/allsky/doc/explsup.html>
- Decressin, T., Meynet, G., Charbonnel, C., Prantzos, N., & Ekström, S. 2007, *A&A*, 464, 1029
- François, P., Matteucci, F., Cayrel, R., Spite, M., Spite, F., & Chiappini, C. 2004, *A&A*, 421, 613
- Friel, E. D., Jacobson, H. R., Barrett, E., Fullton, L., Balachandran, S. C., & Pilachowski, C. A. 2003, *AJ*, 126, 2372
- Fulbright, J. P. 2002, *AJ*, 123, 404
- Fulbright, J. P., McWilliam, A., & Rich, R. M. 2006, *ApJ*, 636, 821
- Fulbright, J. P., McWilliam, A., & Rich, R. M. 2007, *ApJ*, 661, 1152
- Gallagher, J.S., III, & Wyse, R.F.G. 1994, *PASP*, 106, 1225
- Geisler, D., Smith, V. V., Wallerstein, G., Gonzalez, G., & Charbonnel, C. 2005, *AJ*, 129, 1428

- Gilmore, G., & Wyse, R. F. G. 1998, *AJ*, 116, 748  
 Gilmore, G. & Wyse, R.F.G. 1991, *ApJ*, 367, L55  
 Gilmore, G., Wilkinson, M.I., Wyse, R.F.G., Kleyna, J.T., Koch, A., Evans, N.W., & Grebel, E.K. 2007, *ApJ*, 663, 948  
 Gonzalez, G., & Wallerstein, G. 1999, *AJ*, 117, 2286  
 Gratton, R., Sneden, C., & Carretta, E. 2004, *ARA&A*, 42, 385  
 Grebel, E. K., & Richtler, T., 1992, *A&A*, 253, 359  
 Grebel, E. K., & Gallagher, J. S., III 2004, *ApJ*, 610, L89  
 Grebel, E. K., Gallagher, J. S., III, & Harbeck, D. 2003, *AJ*, 125, 1926  
 Grevesse, N., & Sauval, A. J. 1999, *A&A*, 347, 348  
 Harbeck, D., et al. 2001, *AJ*, 122, 3092  
 Helmi, A., et al. 2006, *ApJ*, 651, L121  
 Hinkle, K., Wallace, L., Valenti, J., & Harmer, D. 2000, Visible and Near Infrared Atlas of the Arcturus Spectrum 3727-9300Å (San Francisco: ASP), online atlas at <ftp://ftp.noao.edu/catalogs/arcturusatlas/visual/>  
 Israelian, G., García López, R. J., & Rebolo, R. 1998, *ApJ*, 507, 805  
 Ivans, I. I., Sneden, C., James, C. R., Preston, G. W., Fulbright, J. P., Höflich, P. A., Carney, B. W., & Wheeler, J. C. 2003, *ApJ*, 592, 906  
 Johnson, J. A. 2002, *ApJSS*, 139, 219  
 Johnson, J. A., Ivans, I. I., & Stetson, P. B. 2006, *ApJ*, 640, 801  
 Kleyna, J. T., Wilkinson, M. I., Gilmore, G., & Evans, N. W. 2003, *ApJ*, 588, L21  
 Kniazev, A. Y., Grebel, E. K., Pustilnik, S. A., Pramskij, A. G., & Zucker, D. B. 2005, *AJ*, 130, 1558  
 Koch, A., Grebel, E. K., Wyse, R. F. G., Kleyna, J. T., Wilkinson, M. I., Harbeck, D. R., Gilmore, G. F., & Evans, N. W. 2006, *AJ*, 131, 895 (Paper I)  
 Koch, A., Grebel, E. K., Kleyna, J. T., Wilkinson, M. I., Harbeck, D. R., Wyse, R. F. G., & Evans, N. W., 2007, *AJ*, 133, 270  
 Koch, A., & McWilliam, A. 2008, *AJ*, submitted  
 Kraft, R. P., & Ivans, I.I. 2003, *PASP*, 115, 143  
 Langer, G. E., Hoffmann R. D., Sneden, C. 1993, *PASP*, 105, 301  
 Lanfranchi, G. A., & Matteucci, F. 2004, *MNRAS*, 351, 1338  
 Lanfranchi, G. A., Matteucci, F., & Cescutti, G. 2006a, *MNRAS*, 365, 477  
 Lanfranchi, G. A., Matteucci, F., & Cescutti, G. 2006b, *A&A*, 453, L67 (LMC06)  
 Langer, G. E., & Hoffmann R. D. 1995, *PASP*, 107, 1177  
 Letarte, B., Hill, V., Jablonka, P., Tolstoy, E., & Meylan, G. 2006, *A&A*, 453, 547  
 Luck, R. E., & Bond, H. E. 1985, *ApJ*, 292, L559  
 Mateo, M. 1998, *ARA&A*, 36, 435  
 Majewski, S. R., Ostheimer, J. C., Patterson, R. J., Kunkel, W. E., Johnston, K. V., & Geisler, D. 2000, *AJ*, 119, 760  
 Matteucci, F., & Greggio, L. 1986, *A&A* 154, 279  
 Matteucci, F. 2003, *Ap&SS*, 284, 539  
 McWilliam, A., Preston, G. W., Sneden, C. & Searle, L. 1995, *AJ*, 109, 275  
 McWilliam, A. 1997, *ARA&A*, 35, 503  
 Mighell, K.J. 1997, *AJ*, 114, 1458  
 Miller, G. E., & Scalo, J. M. 1979, *ApJS*, 41, 513  
 Mishenina, T. V., Korotin, S. A., Klochkova, V. G., & Panchuk, V. E. 2000, *A&A*, 353, 978  
 Monaco, L., Bellazzini, M., Bonifacio, P., Ferraro, F. R., Marconi, G., Pancino, E., Sbordone, L., & Zaggia, S. 2005, *A&A*, 441, 141  
 Monelli, M., et al. 2003, *AJ*, 126, 218  
 Nissen, P. E., & Schuster, W. J. 1997, *A&A*, 326, 751  
 Nonino, M., et al. 1999, *A&AS*, 137, 51  
 Norris, J. E., Ryan, S. G., Beers, T. C., Aoki, W., & Ando, H. 2002, *ApJ*, 569, L107  
 O'Brian, T. R., Wickliff, M. E., Lawler, J. E., Whaling, W., & Brault, J. W. 1991, *J. Opt. Soc. Am. B.*, 8, 1185  
 Peterson, R. C., Dalle Ore, C. M., & Kurucz, R. L. 1993 *ApJ*, 404, 333  
 Pont, F., Zinn, R., Gallart, C., Hardy, E., & Winnick, R. 2004, *AJ*, 127, 840  
 Pritzl, B. J., Venn, K. A., & Irwin, M. I. 2005, *AJ*, 130, 2140  
 Prochaska, J. X., Naumov, S. O., Carney, B. W., McWilliam, A., & Wolfe, A. M. 2000, *AJ*, 120, 2153  
 Rizzi, L., Held, E. V., Bertelli, G., & Saviane, I. 2003, *ApJ*, 589, L85  
 Rutledge, G. A., Hesser, J.E., Stetson, P.B., Mateo, M., Simard, L., Bolte, M., Friel, E.D., & Copin, Y. 1997a, *PASP*, 109, 883  
 Rutledge, G.A., Hesser, J.E., Stetson, P.B. 1997b, *PASP*, 109, 907  
 Sadakane, K., Arimoto, N., Ikuta, C., Aoki, W., Jablonka, P., & Tajitsu, A. 2004, *PASJ*, 56, 1041  
 Salaris, M., Chieffi, A., & Straniero, O. 1993, *ApJ*, 414, 580  
 Schlegel, D.J., Finkbeiner, D.P., & Davis, M. 1998, *ApJ*, 500, 525  
 Shetrone, M. D., Côté, P., & Sargent, W. L. W. 2001, *ApJ*, 548, 592  
 Shetrone, M. D., Venn, K. A., Tolstoy, E., Primas, F., Hill, V., & Kaufer, A. 2003, *AJ*, 125, 684 (S03)  
 Sivarani, T., et al. 2004, *A&A*, 413, 1073  
 Smecker-Hane, T.A., Stetson, P.B., Hesser, J.E., & Lehnert, M.D. 1994, *AJ*, 108, 507  
 Smecker-Hane, T. A., Stetson, P. B., Hesser, J. E., & Vandenberg, D. A. 1996, in *From Stars to Galaxies: the Impact of Stellar Physics on Galaxy Evolution*, ASP Conf. Ser. Vol 98, eds. C. Leitherer, U. Fritze-von Alvensleben, & J. Huchra (San Francisco: ASP), 328  
 Smecker-Hane, T.A., Mandushev, G.I., Hesser, J.E., Stetson, P.B., Da Costa, G.S. & Hatzidimitriou, D. 1999, in *Spectrophotometric Dating of Stars and Galaxies*, ASP Conf. Ser. Vol. 192, eds. I. Hubeny, S. Heap, & R. Cornett (San Francisco: ASP), 159  
 Sneden, C. 1973, *ApJ*, 184, 839  
 Thielemann, F.-K., Nomoto, K., & Hashimoto, M. 1996, *ApJ*, 460, 408  
 Thielemann, F.-K., et al. 2001, *PrPNP*, 46, 5  
 Tinsley, B. 1976, *ApJ*, 208, 797  
 Timmes, F. X., Woosley, S. E., & Weaver, T. A. 1995, *ApJS*, 98, 617  
 Tolstoy, E., Irwin, M.J., Cole, A.A., Pasquini, L., Gilmozzi, R., & Gallagher, J.S. 2001, *MNRAS*, 327, 918  
 Tolstoy, E., Venn, K. A., Shetrone, M. D., Primas, F., Hill, V., Kaufer, A., & Szeifert, T. 2003, *AJ*, 125, 707 (T03)  
 Unavane, M., Wyse, R. F. G., & Gilmore, G. 1996, *MNRAS*, 278, 727  
 Venn, K. A., Irwin, M. I., Shetrone, M. D., Tout, C. A., Hill, V., & Tolstoy, E. 2004, *AJ*, 128, 1177  
 Wilkinson, M. I., Kleyna, J. T., Gilmore, G. F., Evans, N. W., Koch, A., Grebel, E. K., Wyse, R. F. G., & Harbeck, D. 2006, *The ESO Messenger*, 124, 25  
 Woosley, S. E. 1986, in *Nucleosynthesis and Chemical Evolution*, 16th Advanced Course Swiss Society of Astrophysics and Astronomy, ed. B. Hauck, A. Maeder & G. Meynet (Geneva: Geneva Observatory), 74  
 Woosley, S. E., & Weaver, T. A. 1995, *ApJS*, 101, 181  
 Wyse, R. F. G., & Gilmore, G. F. 1988, *AJ*, 95, 1404  
 Wyse, R. F. G., 2002, *New Astron.*, 7, 395  
 Wyse, R. F. G., Gilmore, G., Norris, J. E., Wilkinson, M. I., Kleyna, J. T., Koch, A., Evans, N. W., & Grebel, E. K. 2006, *ApJ*, 639, L13  
 Zhang, H. W., & Zhao, G. 2005, *MNRAS*, 364, 712  
 Zinn, R., & West, M. J. 1984, *ApJS*, 55, 45

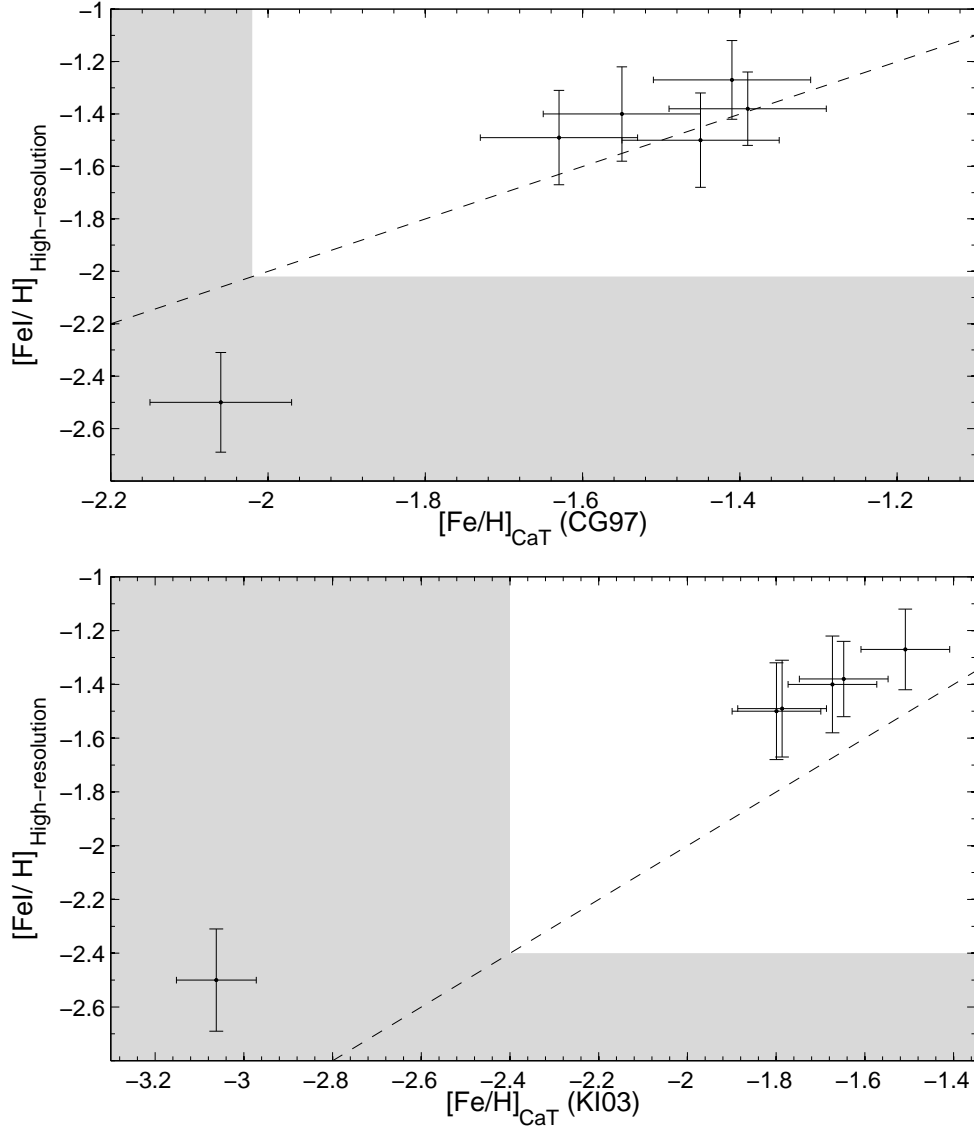


FIG. 1.— Comparison of the metallicities from high- and medium-resolution (CaT) analyses on the metallicity scales of Carretta & Gratton (1997; CG97; top panel) and Kraft & Ivans (2003; KI03; bottom panel). Shown are those six of our target stars, for which CaT widths were measured in Paper I. The horizontal errorbars are formal measurements errors. The  $1\sigma$ -errorbars on  $[\text{Fe}/\text{H}]$  are those deduced in Section 3.3. The grey-shaded areas illustrate the ranges, where the CaT calibrations have to be extrapolated due to the lack of very metal poor calibrating clusters in Rutledge et al. (1997a,b) and Kraft & Ivans (2003).

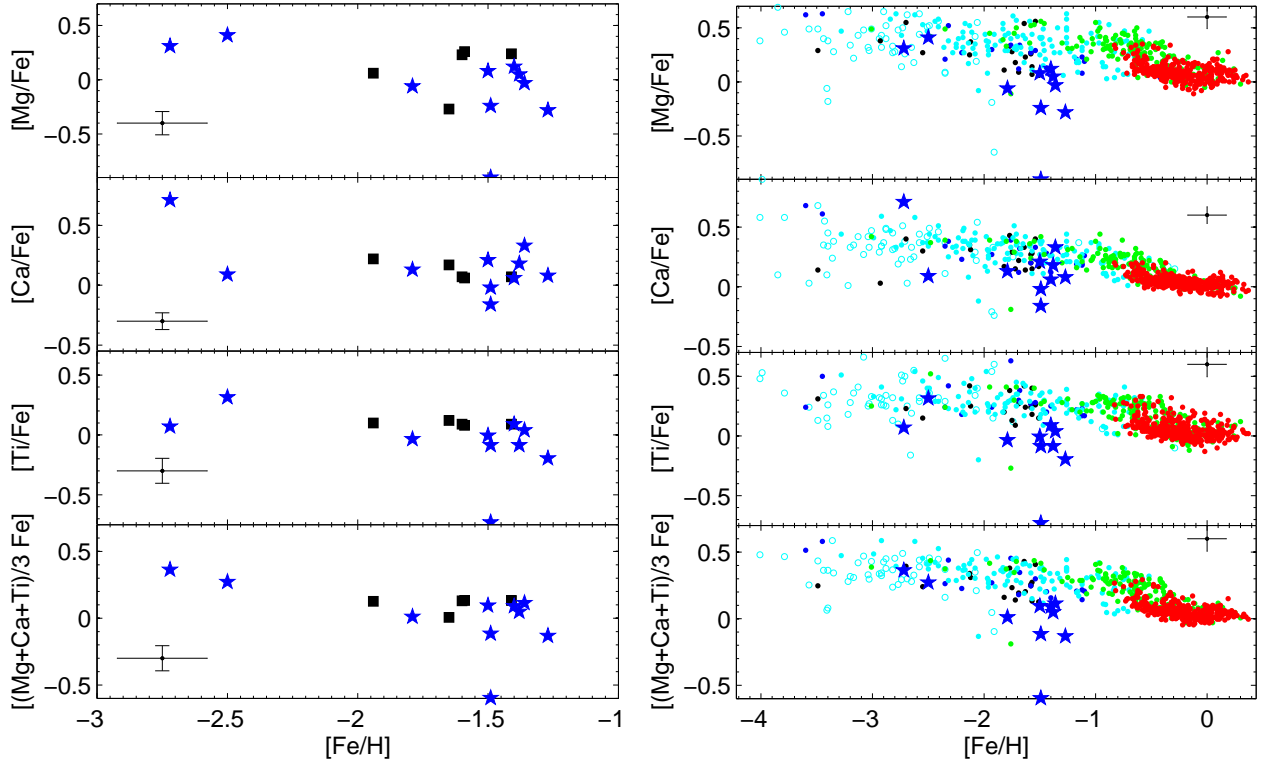


FIG. 2.— Abundance ratios for the  $\alpha$ -elements Mg, Ca and Ti: Our measurements for the ten Carina red giants are shown as filled blue stars, the filled black squares in the left panels are the Carina stars from S03. The additional data points in the right panels are Galactic field stars, where the color coding illustrates the kinematic separation into Galactic components and is shown in analogy to Venn et al. (2004); halo (cyan), thick disk (green), thin disk (red), retrograde orbits (black) and those with a high-velocity Toomre component (blue). For stars shown as open cyan symbols, there is no existing velocity information. The errorbars in the upper right corner are those derived in Section 3.3. [See the electronic edition of the Journal for a color version of this figure.]

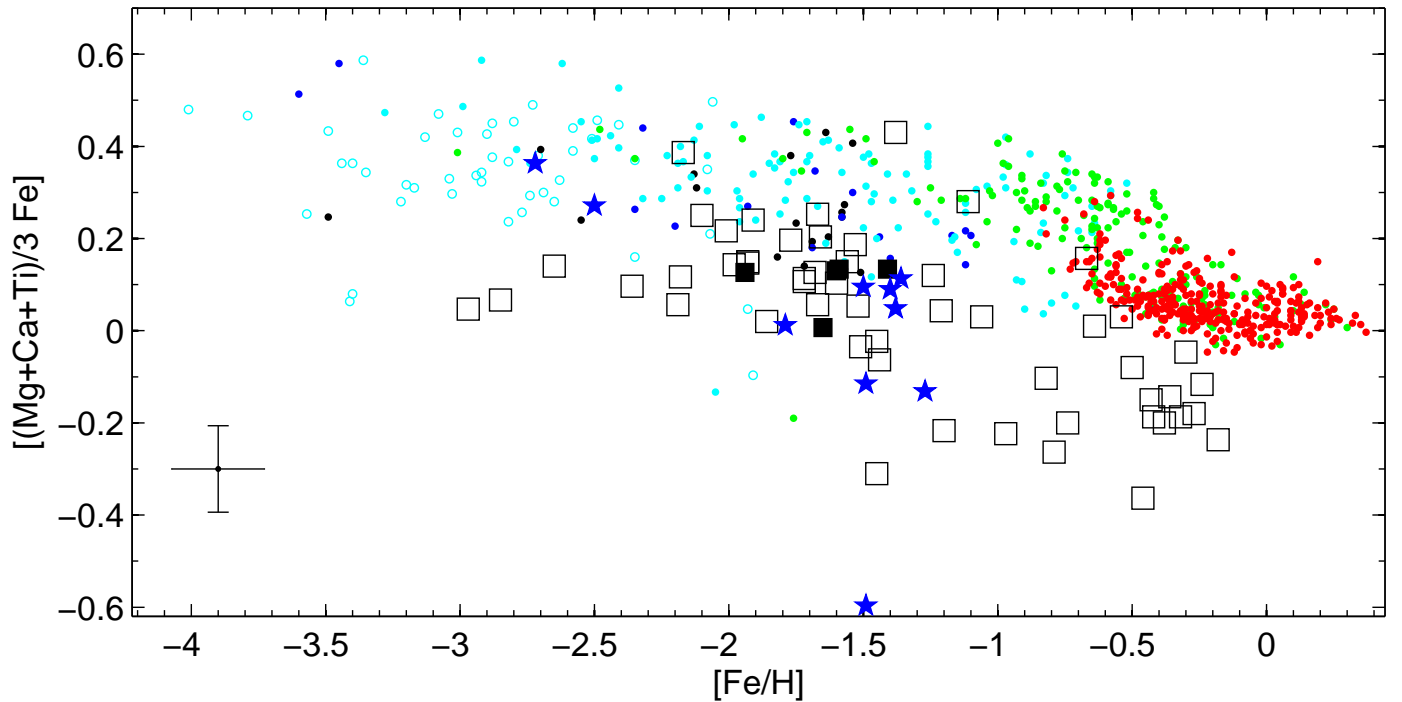


FIG. 3.— Average  $\alpha$  abundance ratio in analogy to Fig. 2. In addition, chemical element data of stars in eight other dSphs are shown as open squares (Shetrone et al. 2001, S03; Sadakane et al. 2004; Geisler et al. 2005; Monaco et al. 2005). [See the electronic edition of the Journal for a color version of this figure.]



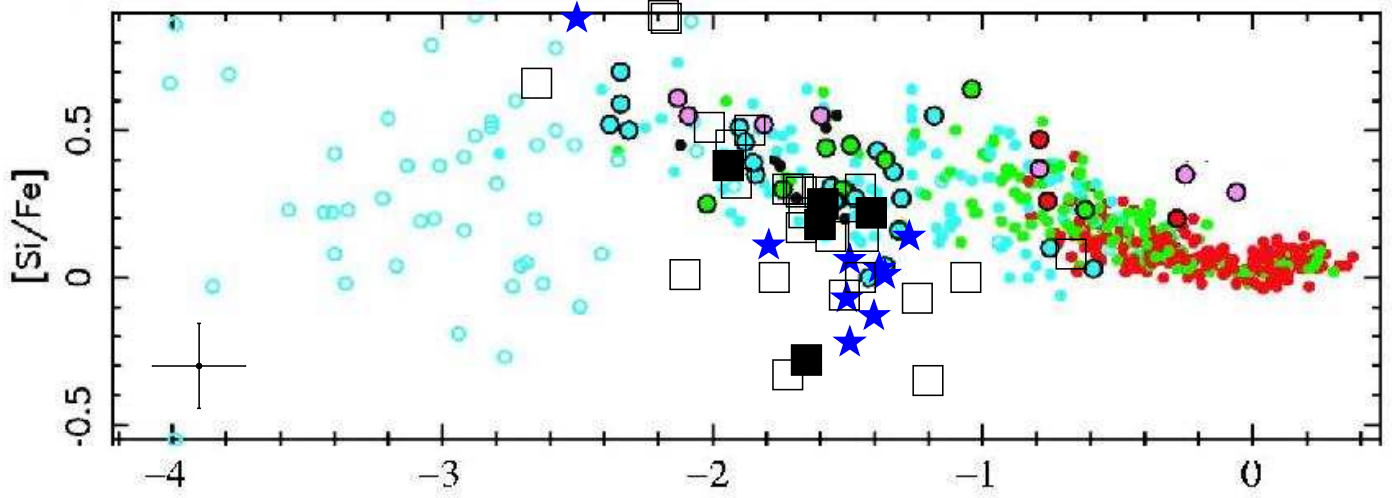


FIG. 4.— Same as Fig. 3, but for silicon abundances. Due to the lack of Si information in Venn et al. (2004), this figure was taken from Pritzl et al. (2005) and additionally displays a sample of globular clusters (filled large circles). Reproduced with kind permission by B. J. Pritzl. [See the electronic edition of the Journal for a color version of this figure.]

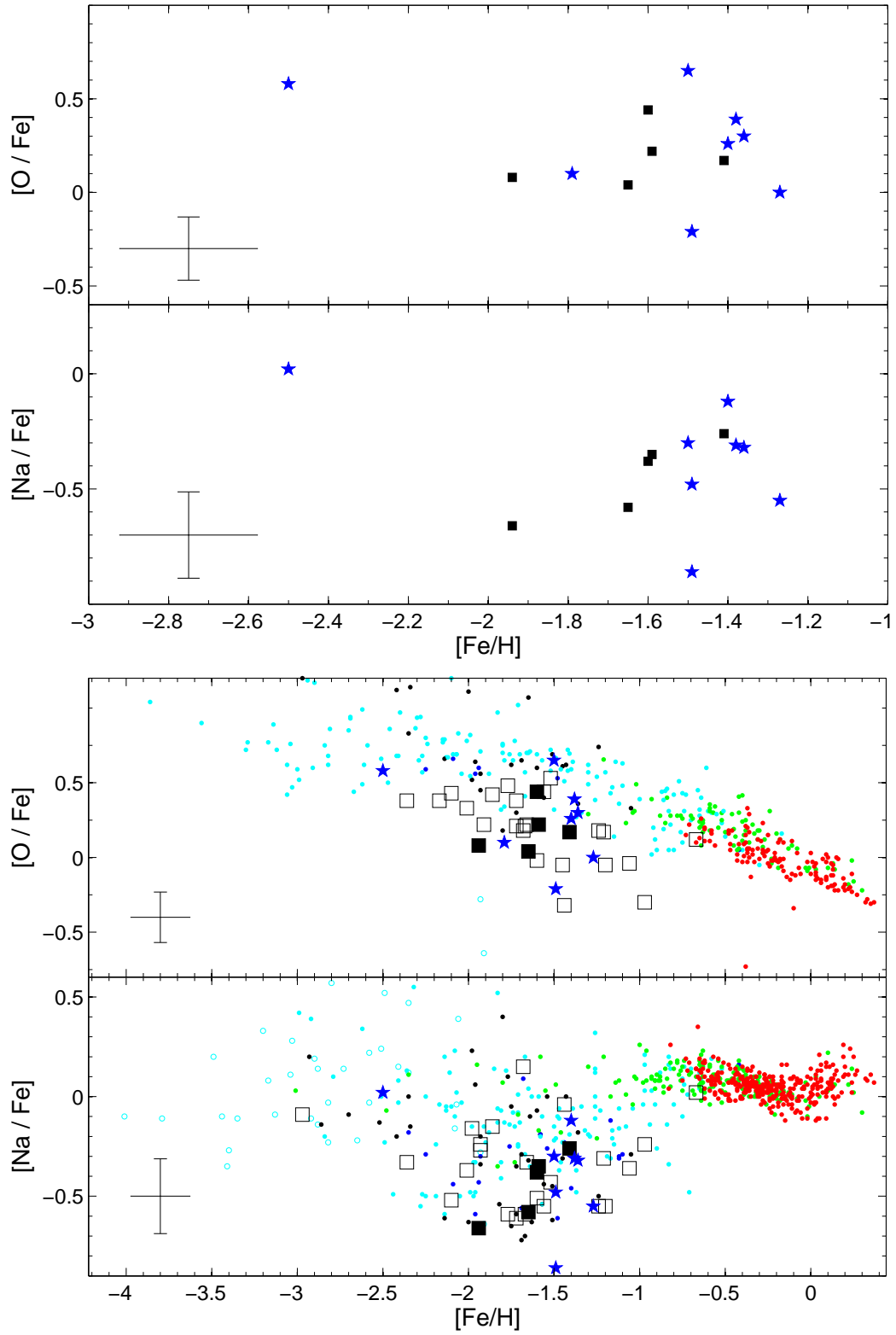


FIG. 5.— Same as Fig. 2, but for Na and O abundances. For illustration, the oxygen data were complemented with halo stars from the samples of Israelian et al. (1998); Boesgaard et al. (1999); Mishenina et al. (2000); Akerman et al. (2004); Bai et al. (2004); Cayrel et al. (2004) and Zhang & Zhao (2005). [See the electronic edition of the Journal for a color version of this figure.]

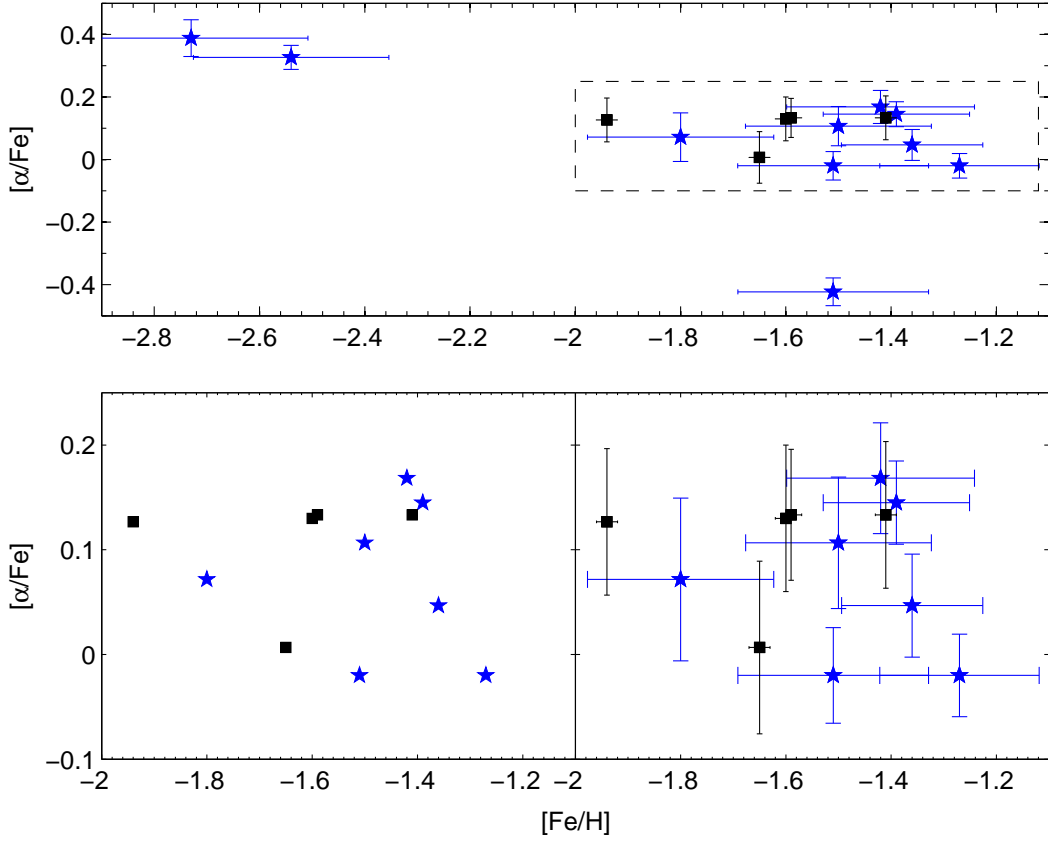


FIG. 6.— Our measured  $[\alpha/\text{Fe}]$  (blue stars) shown together with the data from S03 (black squares). The bottom panels are blow-ups of the region enclosed by the dashed quadrangle in the top panel. In the bottom left panel errorbars were omitted for clarity. [See the *electronic edition of the Journal* for a color version of this figure.]

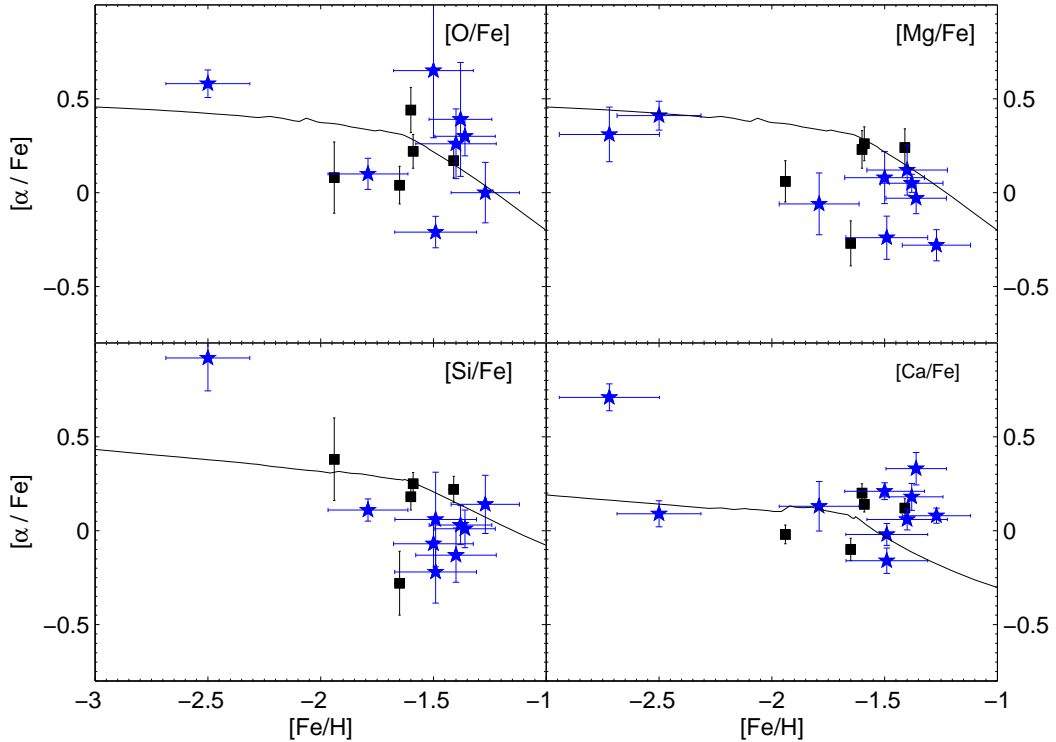


FIG. 7.— Our measured abundance ratios for the  $\alpha$ -elements O, Mg, Si and Ca, shown as blue stars, in comparison with the model calculations from LMC06 (solid lines). Also plotted are the five data points from S03 (black squares). [See the *electronic edition of the Journal* for a color version of this figure.]

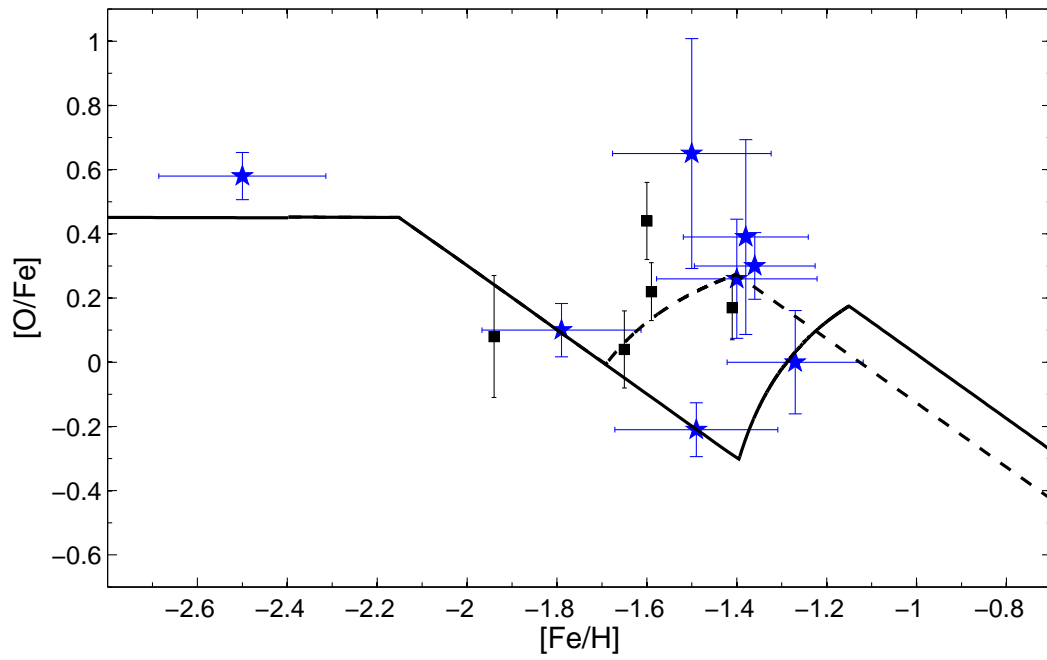


FIG. 8.— Chemical evolution models from Gilmore & Wyse (1991), which incorporate an initial SF burst, an extended quiescent phase, and a second successive burst. The solid and dashed line adopt different onsets of SF. The models were offset by  $-0.4$  dex in  $[Fe/H]$  w.r.t. the original predictions from Gilmore & Wyse (1991) to match the observed element ratios from this work (blue stars) and S03 (black squares). [See the electronic edition of the *Journal* for a color version of this figure.]

TABLE 1  
RADIAL VELOCITY MEMBERS IN CARINA.

Star <sup>a</sup>	$\alpha$ (J2000)	$\delta$ (J2000)	V	B-V	V-K	$v_r$ [km s <sup>-1</sup> ]	S/N
LG04b_004260	06 40 30	-50 59 15	17.75	0.99	3.17	215.6	18
LG04c_006477	06 41 21	-51 03 43	17.71	1.31	2.71	219.5	17
LG04a_000377	06 41 59	-50 51 13	17.78	1.30	3.23	219.5	18
LG04a_001556	06 42 17	-50 55 55	17.82	1.25	3.10	223.1	19
LG04a_001826	06 40 58	-50 53 35	17.76	1.29	2.88	224.8	18
LG04c_000777	06 41 04	-51 01 35	17.55	1.31	3.02	225.1	20
LG04a_002181	06 41 39	-50 49 58	17.62	1.36	2.88	230.6	21
LG04d_006628	06 41 37	-51 01 43	17.95	1.28	2.90	231.1	23
LG04c_000951	06 39 55	-50 57 36	17.79	1.19	2.72	233.2	15
LG04c_000626	06 40 47	-51 06 03	17.60	1.37	3.10	237.6	16

Note. — The given colors are dereddened values in the JC system.

<sup>a</sup>The nomenclature is such that LG04a-d designates the EIS-fields targeting Carina, followed by the number in the respective input catalog (P.Lynam [EIS-team], 2003, private communication).

TABLE 2  
LINELIST

Ion	Wavelength [Å]	EP [eV]	$\log gf$	Equivalent Width [mÅ]										
				Arcturus	4260 <sup>a</sup>	6477 <sup>a</sup>	377 <sup>a</sup>	1556 <sup>a</sup>	1826 <sup>a</sup>	777 <sup>a</sup>	2181 <sup>a</sup>	6628 <sup>a</sup>	951 <sup>a</sup>	626 <sup>a</sup>
Fe I	4802.88	3.69	-1.64	89.8	38.8	35.0	79.3	20.5	37.5	39.6	43.5	21.5	...	...
Fe I	4839.54	3.27	-1.90	102.4	34.0	42.1	69.8	44.6	60.2	54.3	59.5	30.5	29.3	38.1
Fe I	4871.32	2.85	-0.43	246.9	91.8	102.5	120.8	126.6	114.5	125.6	141.1	82.7	74.5	116.2
Fe I	4903.31	2.88	-0.67	206.6	88.9	107.7	109.9	107.9	95.6	97.0	112.4	71.7	36.1	70.2
Fe I	4918.99	2.85	-0.41	250.5	136.1	127.2	142.9	137.5	141.2	151.0	142.4	95.0	74.2	98.4

Note. — This Table is published in its entirety in the electronic edition of the *Astronomical Journal*.

<sup>a</sup>For the sake of readability, only the catalogue-numbers are given here, omitting the prefixes “LG04[abcd]-” (cf. Table 1)

TABLE 3  
SPECTROSCOPIC AND PHOTOMETRIC MODEL ATMOSPHERE PARAMETERS

Star	$T_{\text{eff}}$	$\sigma T_{\text{eff}}$	$T_{\text{eff}}$	$\xi$	$\log g$	[Fe/H]	[M/H]
	Photometric		Spectroscopic	[km/s]	cgs	(CaT)	
LG04b_004260	4091	62	4594	1.52	1.53	-1.63	-1.50
LG04c_006477	4397	80	4600	1.54	1.49	-1.55	-1.42
LG04a_000377	4060	60	4511	1.74	1.39	-1.45	-1.50
LG04a_001556	4134	64	4570	1.75	1.68	-1.41	-1.30
LG04a_001826	4271	73	4384	1.74	0.84	...	-1.46
LG04c_000777	4183	67	4205	1.25	0.85	...	-1.38
LG04a_002181	4279	73	4317	1.66	1.26	-1.39	-1.39
LG04d_006628	4260	72	4717	1.40	2.02	...	-1.81
LG04c_000951	4387	80	4395	1.66	0.90	...	-2.74
LG04c_000626	4130	64	4420	1.70	1.80	-2.06	-2.57

TABLE 4  
 ERROR ANALYSIS FOR TWO REPRESENTATIVE STARS – UNCORRELATED CONTRIBUTIONS

Ion	$\Delta T_{\text{eff}}$		$\Delta \log g$		$\Delta \xi$		$\Delta [M/H]$		$\alpha$
	+100 K	-100 K	+0.2	-0.2	+0.1	-0.1	+0.2	-0.2	
LG04c_000777									
O I	-0.010	0	+0.090	-0.080	-0.010	0	+0.060	-0.070	+0.080
Na I	+0.090	-0.095	-0.035	+0.040	-0.010	+0.015	-0.025	+0.045	-0.045
Mg I	-0.039	+0.028	-0.018	+0.017	+0.049	-0.051	-0.012	+0.011	-0.036
Si I	-0.132	+0.138	+0.032	-0.033	+0.069	-0.065	+0.025	-0.023	+0.010
Ca I	+0.023	-0.054	-0.025	+0.023	+0.021	-0.021	-0.035	+0.027	-0.037
Ti I	+0.094	-0.125	-0.006	+0.011	+0.033	-0.030	-0.034	+0.029	-0.035
Ti II	-0.130	+0.113	+0.056	-0.059	+0.019	-0.015	+0.041	-0.045	+0.056
Fe I	+0.116	-0.081	-0.002	+0.003	-0.075	+0.075	+0.005	-0.001	+0.040
Fe II	-0.112	+0.162	+0.065	-0.070	-0.053	+0.058	+0.070	-0.062	+0.125
LG04d_006628									
O I	-0.010	+0.010	+0.080	-0.090	0	0	+0.070	-0.070	+0.090
Na I	...	...	...	...	...	...	...	...	...
Mg I	-0.040	+0.054	-0.011	+0.023	+0.010	-0.003	+0.006	-0.006	+0.012
Si I	-0.110	+0.114	+0.029	-0.027	+0.040	-0.043	+0.016	-0.026	+0.032
Ca I	-0.044	+0.039	-0.001	+0.003	+0.020	-0.020	+0.006	-0.009	+0.001
Ti I	+0.022	-0.041	-0.005	-0.003	+0.024	-0.025	-0.001	+0.005	-0.015
Ti II	-0.115	+0.136	+0.096	-0.082	0	0	+0.056	-0.064	+0.092
Fe I	+0.140	-0.134	-0.019	+0.017	-0.040	+0.043	-0.016	+0.026	-0.022
Fe II	0	+0.051	+0.084	-0.067	-0.023	+0.021	+0.034	-0.034	+0.063

TABLE 5  
ABUNDANCE RESULTS FOR THE ANALYSED CARINA RED GIANTS

Element	LG04a_002181				LG04b_004260				LG04c_006477			
	[X/Fe]	$\sigma_{EW}$	N	$\sigma_{tot}$	[X/Fe]	$\sigma_{EW}$	N	$\sigma_{tot}$	[X/Fe]	$\sigma_{EW}$	N	$\sigma_{tot}$
O I	0.39	0.40	2	0.30	-0.21	0.05	1	0.08	0.26	0.24	2	0.19
Na I	-0.31	0.39	2	0.29	-0.86	0.05	1	0.10	-0.12	0.38	3	0.24
Mg I	0.05	0.03	2	0.05	-0.24	0.13	2	0.11	0.12	0.18	2	0.13
Si I	0.03	0.10	4	0.10	-0.22	0.13	2	0.17	-0.13	0.05	1	0.14
Ca I	0.18	0.04	18	0.07	-0.02	0.07	15	0.06	0.06	0.08	16	0.06
Ti I	-0.12	0.04	32	0.12	-0.17	0.06	16	0.09	0.13	0.07	18	0.09
Ti II	-0.05	0.11	6	0.11	0.00	0.07	5	0.02	0.05	0.05	5	0.10
Fe I/H	-1.38	0.22	97	0.14	-1.49	0.16	96	0.18	-1.40	0.16	97	0.18
Fe II/H	-1.38	0.18	7	0.27	-1.48	0.13	4	0.20	-1.37	0.12	6	0.19

Element	LG04a_000377				LG04a_001556				LG04a_001826			
	[X/Fe]	$\sigma_{EW}$	N	$\sigma_{tot}$	[X/Fe]	$\sigma_{EW}$	N	$\sigma_{tot}$	[X/Fe]	$\sigma_{EW}$	N	$\sigma_{tot}$
O I	0.65	0.50	2	0.36	0.00	0.20	2	0.16	...	...	...	...
Na I	-0.30	0.40	2	0.29	-0.55	0.21	2	0.17	-0.48	0.06	1	0.11
Mg I	0.08	0.19	2	0.14	-0.28	0.10	2	0.08	-0.90	0.06	1	0.09
Si I	-0.07	0.06	1	0.14	0.14	0.17	2	0.15	0.06	0.28	2	0.25
Ca I	0.21	0.04	17	0.04	0.08	0.07	16	0.04	-0.16	0.05	15	0.07
Ti I	0.07	0.06	26	0.08	-0.22	0.05	28	0.20	-0.83	0.08	16	0.12
Ti II	-0.08	0.07	5	0.23	-0.17	0.13	6	0.11	-0.63	0.11	5	0.08
Fe I/H	-1.50	0.16	91	0.18	-1.27	0.14	98	0.15	-1.49	0.16	95	0.18
Fe II/H	-1.49	0.12	5	0.20	-1.29	0.14	7	0.23	-1.43	0.14	7	0.22

Element	LG04c_000777				LG04d_006628				LG04c_000951			
	[X/Fe]	$\sigma_{EW}$	N	$\sigma_{tot}$	[X/Fe]	$\sigma_{EW}$	N	$\sigma_{tot}$	[X/Fe]	$\sigma_{EW}$	N	$\sigma_{tot}$
O I	0.30	0.08	1	0.10	0.10	0.06	1	0.08	...	...	...	...
Na I	-0.32	0.13	2	0.12	...	...	...	...	...	...	...	...
Mg I	-0.03	0.20	2	0.08	-0.06	0.13	1	0.16	0.31	0.12	1	0.15
Si I	0.01	0.24	3	0.10	0.11	0.04	1	0.06	...	...	...	...
Ca I	0.33	0.06	17	0.09	0.13	0.10	11	0.13	0.71	0.05	9	0.07
Ti I	-0.09	0.06	29	0.08	-0.25	0.08	11	0.14	0.10	0.14	8	0.09
Ti II	0.17	0.15	5	0.15	0.18	0.17	4	0.14	0.04	0.12	3	0.10
Fe I/H	-1.36	0.12	90	0.13	-1.79	0.15	86	0.18	-2.72	0.16	67	0.22
Fe II/H	-1.35	0.19	4	0.29	-1.79	0.12	7	0.14	-2.72	0.12	4	0.13

Element	LG04c_00626			
	[X/Fe]	$\sigma_{EW}$	N	$\sigma_{tot}$
O I	0.58	0.05	1	0.07
Na I	0.02	0.05	1	0.10
Mg I	0.41	0.09	2	0.08
Si I	0.92	0.13	2	0.18
Ca I	0.09	0.11	9	0.07
Ti I	0.23	0.05	9	0.10
Ti II	0.40	0.08	3	0.03
Fe I/H	-2.50	0.15	79	0.19
Fe II/H	-2.54	0.11	4	0.16